Eremane, viscidane and isozizaene diterpenoids from the leaves of Eremophila rigida and their absolute configurations

Liang, Chao; Ndi, Chi; Semple, Susan J.; Buirchell, Bevan; Coriani, Sonia; Møller, Birger Lindberg; Staerk, Dan

Published in:
Phytochemistry

Link to article, DOI:
10.1016/j.phytochem.2024.113972

Publication date:
2024

Document Version
Publisher's PDF, also known as Version of record

Phytochemistry 219 (2024) 113972

Contents lists available at ScienceDirect

Phytochemistry

journal homepage: www.elsevier.com/locate/phytochem

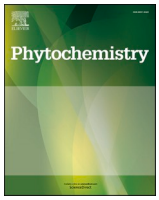

Eremane, viscidane and isozizaene diterpenoids from the leaves of *Eremophila rigida* and their absolute configurations

Chao Liang [a], Chi Ndi [b], Susan J. Semple [b], Bevan Buirchell [c], Sonia Coriani [d], Birger Lindberg Møller [e], Dan Staerk [a,*]

[a] Department of Drug Design and Pharmacology, Faculty of Health and Medical Sciences, University of Copenhagen, Universitetsparken 2, DK-2100, Copenhagen, Denmark
[b] Quality Use of Medicines and Pharmacy Research Centre, Clinical and Health Sciences, University of South Australia, Frome Road, Adelaide, 5000, Australia
[c] Wise Owl Consulting, Como, Western Australia, 6152, Australia
[d] Department of Chemistry, Technical University of Denmark, Kemitorvet Building 207, DK-2800, Kongens Lyngby, Denmark
[e] Plant Biochemistry Laboratory, Department of Plant and Environmental Sciences, University of Copenhagen, Thorvaldsensvej 40, DK-1871, Frederiksberg C, Denmark

ARTICLE INFO

Keywords:
Eremophila rigida Chinnock
Scrophulariaceae
High-resolution inhibition profiling
Eremane diterpenoid
Viscidane diterpenoid
Isozizaene diterpenoid
Protein tyrosine phosphatase 1B inhibitors

ABSTRACT

Previously undescribed eremane, viscidane, and isozizaene diterpenoids, eremorigidanes A-F, along with six known *O*-methylated flavonoids and three known triterpenoids were isolated and identified from the leaves of *Eremophila rigida* Chinnock by combined use of high-resolution PTP1B inhibition profiling, semipreparative- and analytical-scale HPLC separations, HPLC-PDA-HRMS analysis, and NMR spectroscopy. The absolute configuration of the unreported diterpenoids were determined by comparison of their experimental and calculated ECD spectra as well as by biosynthetic arguments. All isolates were evaluated for their PTP1B inhibitory activities, which revealed the flavonoid penduletin (**3**) to show inhibition with an IC_{50} value of 18.3 μM, and the triterpenoids 3,4-*seco*-olean-12-ene-3,28-dioic acid (**15**), oleanolic acid (**16**), and 3-oxo-oleanolic acid (**17**) to show inhibition with IC_{50} values of 55.7, 9.9, and 6.3 μM, respectively. The preliminary structure-activity relationship (SAR) of isolated flavonoids and triterpenoids is discussed. Plausible biosynthetic steps involved in eremane and isozizaene metabolism are presented and discussed.

1. Introduction

Diabetes mellitus, as one of the priority non-communicable diseases, has affected 537 million people worldwide and caused 966 billion USD as global healthcare expenditure in 2021 (International Diabetes Federation, 2021). Furthermore, the incidence of diabetes is estimated to rise if no effort is made to control this global epidemic (International Diabetes Federation, 2021). Type 2 diabetes (T2D) which accounts for more than 90% of all diabetes cases, is characterized by chronic hyperglycemia and partial insulin resistance (American Diabetes Association, 2010). T2D is mainly caused by pancreatic β-cells dysfunction and/or insulin resistance in skeletal muscle, liver, and adipose tissue (Lebovitz, 1999; Chatterjee et al., 2017). Drug treatment remains an important and promising therapeutic strategy for T2D. Protein tyrosine phosphatase 1B (PTP1B), as a T2D therapeutic target, dephosphorylates insulin receptor as well as insulin receptor substrate via interaction with and removal of tyrosine phosphates (Johnson et al., 2002). Therefore, PTP1B is capable of downregulating insulin transduction signaling, which leads to a decreased insulin sensitivity. Inhibition of PTP1B thus seems to be an effective strategy for T2D therapy, even though there are still no PTP1B inhibitors approved for clinical use on market. The major challenges for development of current PTP1B inhibitors as T2D drugs are poor selectivity and bioavailability (Liu et al., 2003; De Munter et al., 2012).

The *Eremophila* genus, which belongs to the family Scrophulariaceae, is endemic to Australia and comprises over 200 species (Chinnock, 2007). The name *Eremophila* comes from the Greek language in which eremo means 'desert' and phila 'love', indicating that plant species of this genus prefer to grow within arid or semi-arid regions, and are drought tolerant (Richmond and Ghisalberti, 1994). Phytochemical studies of this genus have identified a wide range of natural products, including fatty acids, flavonoids, lignans, sesquiterpenoids, diterpenoids and triterpenoids (Singab et al., 2013). Diterpenoids are among the most diversified secondary metabolites in *Eremophila*, and includes e.g.,

* Corresponding author.
E-mail address: ds@sund.ku.dk (D. Staerk).

https://doi.org/10.1016/j.phytochem.2024.113972
Received 1 August 2023; Received in revised form 2 January 2024; Accepted 6 January 2024
Available online 10 January 2024

serrulatane, decipiane, cembrene, viscidane, and eremane type diterpenoids with a high degree of structural uniqueness. Crude extracts and/or isolated compounds from *Eremophila* have been reported to show antifungal (Hossain et al., 2019), antibacterial (Barnes et al., 2013; Algreiby et al., 2018; Biva et al., 2019), and antidiabetic activities (Tahtah et al., 2016; Wubshet et al., 2016; Zhao et al., 2019; Pedersen et al., 2020; Liang et al., 2023a, 2023b).

Eremophila rigida Chinnock is an erect shrub which grows to a height of 0.5–1.2 m (Chinnock, 2007; Brown and Buirchell, 2011). The name *rigida* derives from the Latin language, meaning rigid, hard, or inflexible, which particularly refers to the thick and rigid nature of the leaves of this plant (Brown, 1956; Chinnock, 2007). The distribution of this species is restricted to Western Australia, and it mainly habitats on stony clay flats between Meekatharra and Newman in the Gascoyne and Pilbara biogeographic regions (Chinnock, 2007; Brown and Buirchell, 2011). *E. rigida* is highly drought tolerant, but moderately frost tolerant (Boschen et al., 2008). There have not been any phytochemical and pharmacological investigations of *E. rigida* before.

The use of high-resolution inhibition profiling in combination with hyphenated separation and spectroscopic technique, e.g., HPLC-PDA-HRMS or HPLC-PDA-HRMS-SPE-NMR, provides an efficient platform for natural product-based drug discovery. In recent years, the use of this platform in our laboratory has significantly accelerated the identification of α-glucosidase inhibitors (Malik et al., 2020; Liang et al., 2020, 2021, 2023a), α-amylase inhibitors (Zhao et al., 2018; Chu et al., 2019), and PTP1B inhibitors (Zhao et al., 2019; Pedersen et al., 2020; Liang et al., 2020, 2021, 2023a, 2023b) from complex crude extracts of plants, functional foods and endophytes. As part of our ongoing search for structurally unique natural products with antidiabetic potential, high-resolution PTP1B inhibition profiling combined with HPLC-PDA-HRMS was used to identify PTP1B inhibitors from a PTP1B-inhibiting acetonitrile extract of *E. rigida*.

2. Results and discussion

Freeze-dried acetonitrile extract of *Eremophila rigida* leaves redissolved to a test-concentration of 50 μg/mL, showed 93.3 ± 1.9 % inhibition against PTP1B, 24.6 ± 2.9 % inhibition against α-glucosidase, and 3.7 ± 0.6 % inhibition against α-amylase (Table 1). Due to the weak α-glucosidase and α-amylase inhibition, the inhibition of these two enzymes were not investigated further. However, the strong PTP1B inhibition promoted us to assess dose-dependent inhibitory effects of the extract against PTP1B, which led to an IC_{50} value of 21.1 ± 0.9 μg/mL (Table 1, Supplementary data Fig. S1).

2.1. High-resolution PTP1B inhibition profiling of the crude leaf extract and isolation of compounds

The crude acetonitrile extract of *E. rigida* was separated by analytical-scale HPLC using a gradient elution profile of 50 min. The eluate in the retention time range 11–42 min was fractionated onto 88 wells of a 96-well microplate, whereafter the content in each well was evaporated to dryness and assayed for PTP1B inhibitory activity. The results, represented as percent inhibition, were plotted at the average collection time of each well, to provide a high-resolution PTP1B inhibition profile (biochromatogram) with a resolution of 2.05 data points per min (Fig. 1). The biochromatogram shows that HPLC peaks *14* and *17* are correlated with PTP1B inhibitory activity.

Initially, semipreparative-scale HPLC separation of 16 injections of crude extract led to automated collection of **1**, **2**, **3**, **4**, **5**, **6**, **8**, **11**, **13**, **15**, **16**, and **17**. Subsequently, analytical-scale HPLC separation of the material eluted with peaks *7*, *9*, *10*, *12*, and *14* led to isolation of **7a**, **7b**, **9**, **10**, **12a-e**, **14a**, mixture of **14a** and **14b**, and **14c** (Supplementary data Figs. S2–S5).

Table 1
Inhibitory activity of *E. rigida* acetonitrile extract against PTP1B, α-glucosidase, and α-amylase.

Enzyme	Inhibition at 50 μg/mL (%)[a]	IC_{50} (μg/mL)[a]
PTP1B	93.3 ± 1.9	21.1 ± 0.9
α-Glucosidase	24.6 ± 2.9	–
α-Amylase	3.7 ± 0.6	–

[a] Results presented as mean value ± standard error of three independent experiments.

2.2. Identification of known flavonoids and triterpenoids and unidentified metabolites

Comparison of NMR data of isolated pure compounds with those reported in literature identified six known *O*-methylated flavonoids, which were 6-methoxykaempferol 3-methyl ether (**1**) (Forgo et al., 2012), penduletin (**3**) (Amina et al., 2018), casticin (**4**) (Kim et al., 2020), kumatakenin (**6**) (Simpson et al., 2011), santin (**7b**) (Hwang et al., 2019), 5-hydroxy-3,4′,6,7-tetramethoxyflavone (**10**) (Mai et al., 2015), together with three known triterpenoids, which were 3, 4-*seco*-olean-12-ene-3,28-dioic acid (**15**) (Caldwell et al., 2000), oleanolic acid (**16**) (Liang et al., 2020) and 3-oxo-oleanolic acid (**17**) (Wang et al., 2020). For known compounds, the structures, HRMS and NMR data are provided in Supplementary data Table S1. The structures of **5**, **8**, **11**, **12a-12e**, and **13** were not established due to a very low amount or insufficient purity of the isolated material.

2.3. Structure elucidation of previously undescribed eremane, viscidane and isozizaene type diterpenoids

The material eluted with peak *14a* was assigned the molecular formula $C_{20}H_{34}O_3$ on the basis of an $[M-H]^-$ ion observed at *m/z* 321.2426 (calcd for $C_{20}H_{33}O_3^-$ 321.2435, ΔM +2.9 ppm) in the HRMS spectrum (Supplementary data Fig. S9), which corresponds to four indices of hydrogen deficiency. The ^{13}C NMR spectrum (Supplementary data Fig. S30) displayed 20 resonances, of which one was monooxygenated (δ_C 82.3, C-5) and one was a carbonyl group (δ_C 182.9, C-20). The ^1H NMR spectrum (Supplementary data Fig. S29) of **14a** showed the presence of two methyl doublets at δ_H 0.93 (3H, d, $J = 6.8$ Hz, H_3-12) and δ_H 1.14 (3H, d, $J = 7.0$ Hz, H_3-19) as well as two methyl singlets at δ_H 1.07 (3H, s, H_3-13) and δ_H 0.95 (3H, s, H_3-14). Examination of 2D NMR spectroscopic data indicated that **14a** is an eremane diterpenoid (Fig. 2), which is a characteristic class of diterpenoids exclusively reported from genus *Eremophila* to date (Croft et al., 1984; Carroll et al., 1985; Ghisalberti et al., 1990). The eremane skeleton incorporates a tricyclo [5.2.2.$0^{1,5}$] undecane ring system which accounts for three indices of hydrogen deficiency. The presence of the A ring (five-membered ring) in the eremane skeleton was confirmed by the H_2-2↔H_2-3↔H-4↔H_3-12 spin system observed in the DQF-COSY spectrum (Supplementary data Fig. S33) as well as by HMBC correlations from H_3-12 to C-3, C-4 and C-5, and from H_2-2 to C-1, C-5 and C-9 (Fig. 3). The B and C rings (the two fused six-membered rings) were established by the H_2-6↔H-7↔H_2-10↔H_2-11 spin system observed in the DQF-COSY spectrum as well as by HMBC correlations from H-7 to C-5, from H-9 to C-1, C-5, C-7, and C-8, and from H_3-13/H_3-14 to C-7, C-8, and C-9 (Fig. 3). The linear side chain, which represents the last indice of hydrogen deficiency, was established on the basis of the H-9↔H_2-15↔H_2-16↔H_2-17↔H-18↔H_3-19 spin system as well as HMBC correlation from H_3-19 to carbonyl C-20 (Fig. 3). The tricyclo [5.2.2.$0^{1,5}$] undecane ring and the linear side chain were assembled by HMBC correlations from H-9 to C-16 (Fig. 3).

ROE correlations between H_3-12 and H-6β, H-6β and H-7, H-7 and H-9, and H-9 and H_3-14 (ROESY spectrum in Supplementary data Fig. S34) placed these protons on the same plane of the molecule (arbitrarily assigned the β configuration), whereas a ROE correlation between H-4 and H_2-11, H_2-11 and H_3-13, H_3-13 and H-15a, and H-15a and H_2-10,

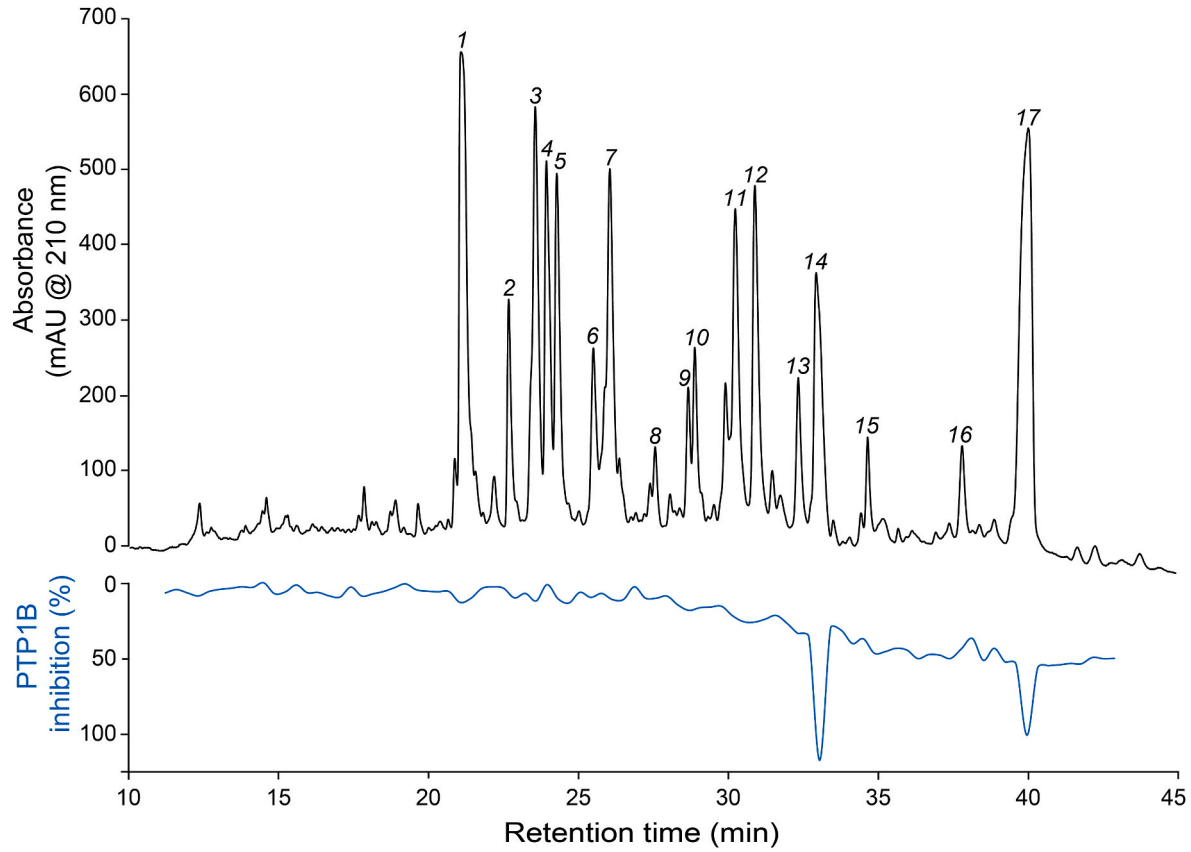

Fig. 1. HPLC chromatogram recorded at 210 nm (black) and high-resolution PTP1B inhibition profile (blue) of acetonitrile extract of *Eremophila rigida*.

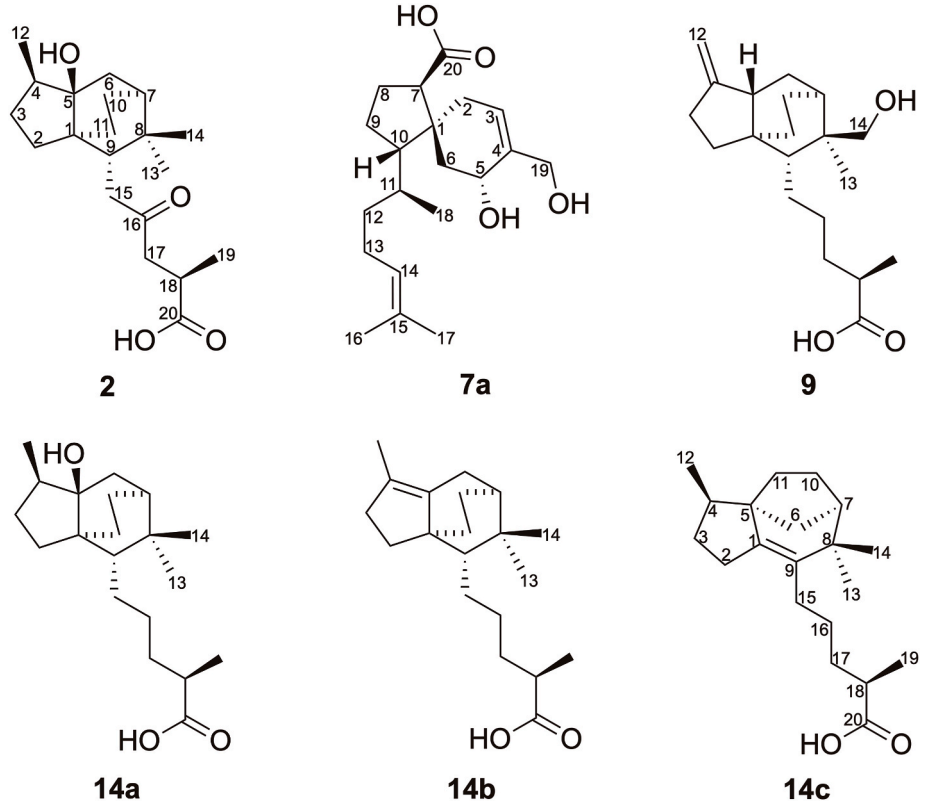

Fig. 2. Structures of previously undescribed eremane, viscidane and isozizaene type diterpenoids from the acetonitrile extract of *Eremophila rigida*.

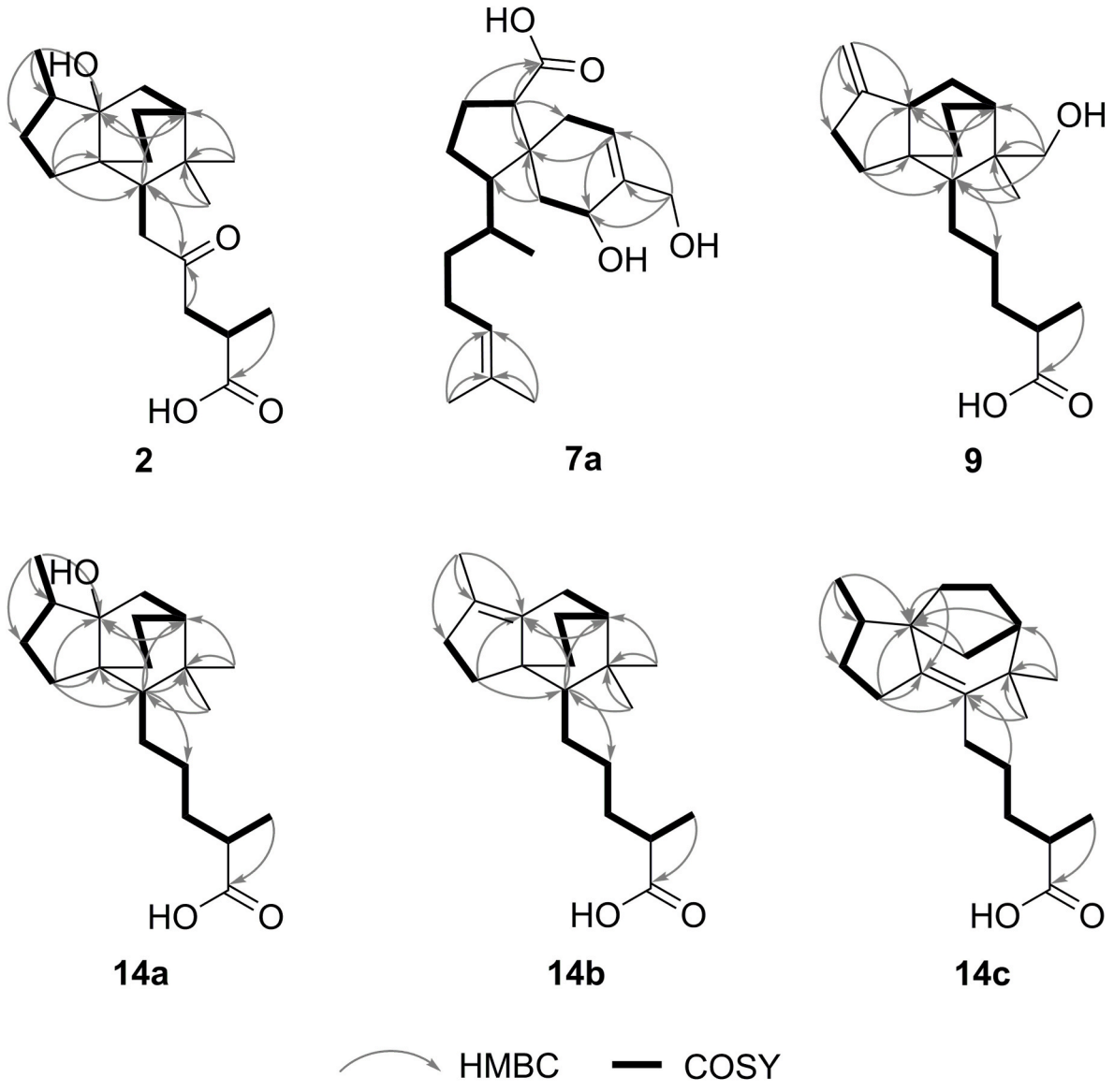

Fig. 3. Selected HMBC and COSY correlations of previously undescribed eremane, viscidane and isozizaene type diterpenoids.

placed these below the plane (α configuration). These correlations established the relative configuration of **14a** as shown in Fig. 4.

Although many attempts were made, production of single crystals for X-ray crystallographic analysis of **14a** unfortunately failed. The absolute configuration of this previously undescribed eremane diterpenoid was therefore determined by comparison of experimental and calculated electronic circular dichroism (ECD) spectra. To considerably reduce the computational time caused by the flexibility of the side chain at C-9, ECD calculation was performed for model structure of **14a** (Fig. 5) constructed through truncation of the structural unit on the side chain from C-16 to C-20. In the first step, 3D structures of (1*R*,4*R*,5*R*,7*S*,9*S*)-**14a model** and (1*S*,4*S*,5*S*,7*R*,9*R*)-**14a model** were subjected to conformational searches, which led to eight and nine possible conformers, respectively. Subsequent geometry optimization revealed six dominant conformers with more than 1% of the Boltzmann population for each enantiomer of the **14a model** mentioned above (Supplementary data Tables S10–S13), and ECD spectra were calculated for these. As illustrated in Fig. 5, the experimental ECD spectrum of **14a** was in agreement with the calculated spectrum for the structure of (1*R*,4*R*,5*R*,7*S*,9*S*)-**14a model,** with an enantiomeric similarity index (Δ_{ESI}) of 0.8866, which established the absolute configuration of the tricyclo [5.2.2.0^{1,5}] undecane ring in **14a** to be (1*R*,4*R*,5*R*,7*S*,9*S*). The stereochemistry of C-18 was tentatively assigned as *R*, *i.e.*, the same configuration as that of C-18 in **14c**, which was determined by ECD calculation *vide infra*, because these two diterpenoids are considered to originate from the same biosynthetic precursor. Thus, the structure of **14a** was established to be (*R*)-5-((1*R*,3a*R*,4*S*,6*S*,7a*R*)-7a-hydroxy-1,5,5-trimethyloctahydro-3a,6-ethanoinden-4-yl)-2-methylpentanoic acid, for which the trivial name eremorigidane D is suggested. ^{1}H and ^{13}C NMR data are provided in Table 2, and ^{1}H NMR, ^{13}C NMR, HSQC, HMBC, COSY, and ROESY spectra are provided in Supplementary data Figs. S29–S34.

The material eluted with peak *2* was assigned the molecular formula $C_{20}H_{32}O_4$ on the basis of an $[M-H]^-$ ion observed at *m/z* 335.2215 (calcd for $C_{20}H_{31}O_4^-$ 335.2228, ΔM +3.8 ppm) in the HRMS spectrum (Supplementary data Fig. S6), which corresponds to five indices of hydrogen deficiency. Intensive analysis of NMR spectroscopic data indicated that **2** and **14a** share identical structures for the tricyclo [5.2.2.0^{1,5}] undecane ring and show high structural similarity for the side chain. However, comparison of ^{13}C NMR spectra of **2** and **14a** revealed that the chemical shift of C-16 in **14a** at δ_C 27.9 was downfield-shifted to δ_C 219.8 in **2**. This corresponds to replacement of a methylene

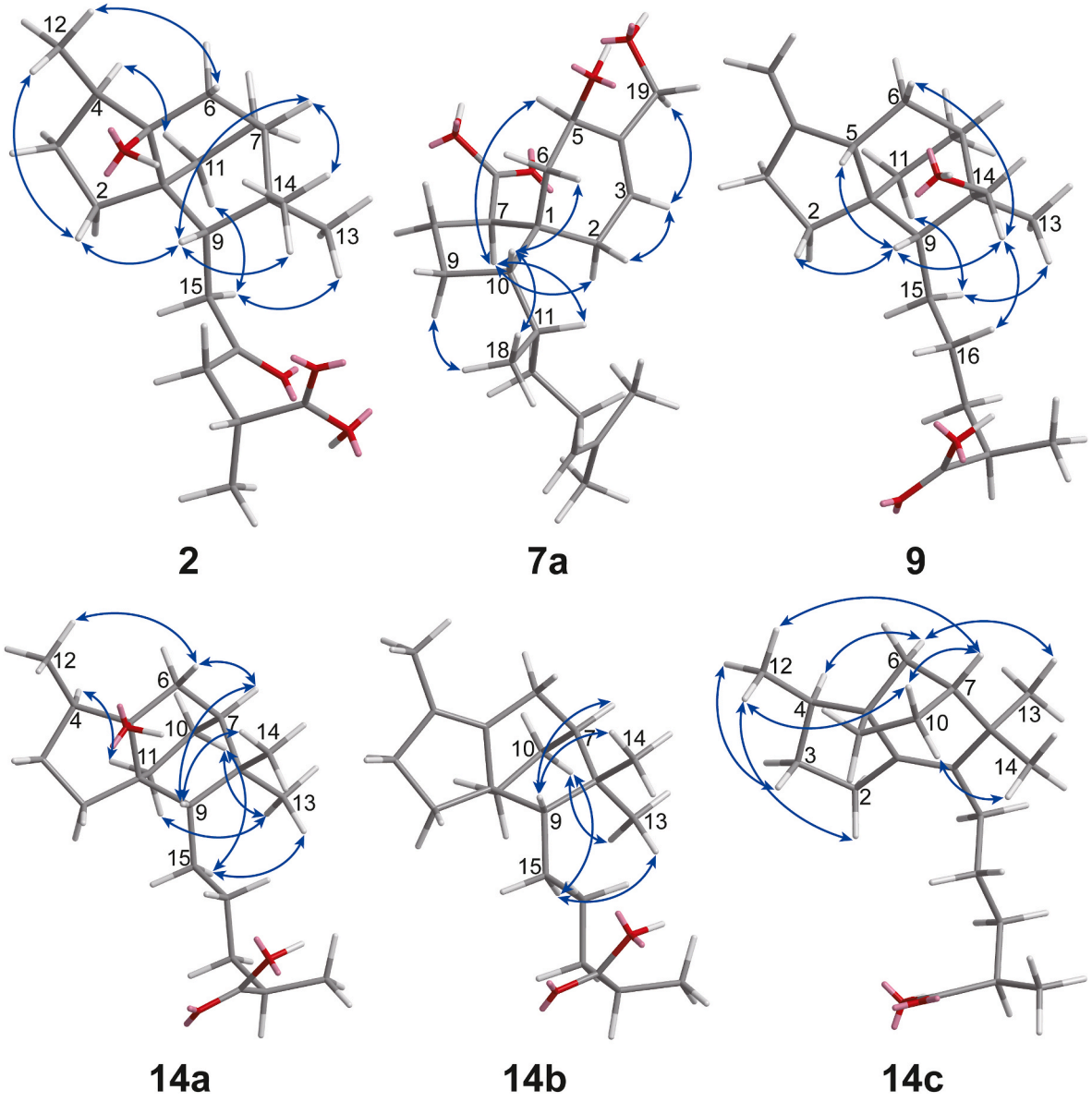

Fig. 4. Key ROESY correlations of previously undescribed eremane, viscidane and isozizaene type diterpenoids.

at C-16 in **14a** with a ketone in **2**, which was confirmed by the disappearance of methylene protons at δ_H 1.06 (1H, overlap, H-16a) and δ_H 1.44 (1H, overlap, H-16b) observed for **14a**, as well as HMBC correlations from H-9 and H_2-17 to the ketone carbon at δ_C 219.8 in **2**.

ROE correlations between H_3-12 and H-2β, H-2β and H-9, H_3-12 and H-6β, H-7 and H-9, and H-9 and H_3-14 suggested H_3-12, H_3-14 and H-9 to be β-oriented, which is consistent with those observed for **14a** (Fig. 4). Furthermore, a ROE correlation between H-15a and H-11α and H_3-13 indicated these to be α-oriented. The relative stereochemistry of the core tricyclic skeleton of **2** and **14a** was therefore established to be identical. The experimental ECD spectra of **2** and **14a** were similar as shown in Supplementary data Fig. S47, concluding **2** to have the same 1*R*,4*R*,5*R*,7*S*,9*S* configuration as **14a**. Similar to **14a**, **2** was tentatively assigned the *R* configuration of C-18 based on biosynthetic arguments. Thus, the structure of **2** was established to be (*R*)-5-((1*R*,3a*R*,4*S*,6-*S*,7a*R*)-7a-hydroxy-1,5,5-trimethyloctahydro-3a,6-ethanoinden-4-yl)-2-methyl-4-oxopentanoic acid, for which the name eremorigidane A is suggested. ^{1}H and ^{13}C NMR data are provided in Table 2, and ^{1}H NMR, ^{13}C NMR, HSQC, HMBC, COSY, and ROESY spectra are provided in Supplementary data Figs. S12–S18.

The material eluted with peak *14b* was assigned the molecular formula $C_{20}H_{32}O_2$ on the basis of an $[M-H]^-$ ion observed at *m/z* 303.2336 (calcd for $C_{20}H_{31}O_2^-$ 303.2329, ΔM −2.1 ppm) in the HRMS spectrum (Supplementary data Fig. S10), which corresponds to five indices of hydrogen deficiency. Analysis of ^{1}H NMR, HSQC and HMBC data proved the material eluted with peak *14b* to be a mixture of the closely related analogs **14a** and **14b** in the ratio 1:2.5. Further attempts to separate **14b** by analytical-scale HPLC using either C_{18} or PFP reversed-phase columns were unsuccessful. Nonetheless, the structures of **14b** (Fig. 2) could be unambiguously established by observing two olefinic quaternary carbons, C-4 at δ_C 125.7 and C-5 at δ_C 140.5, which were assigned by HMBC correlations from H_3-12 to C-3, C-4 and C-5, and from H-2α, H-7, and H-9 to C-5 (Fig. 3).

The experimental ECD data of **14b** was not acquired since it was isolated as a mixture, but **14b** is tentatively assigned to be 1*R*,7*S*,9*S*,18*R* configuration based on biosynthetic arguments. Thus, the structure of **14b** was established to be (*R*)-2-methyl-5-((3a*R*,4*S*,6*S*)-1,5,5-trimethyl-2,3,4,5,6,7-hexahydro-3a,6-ethanoinden-4-yl)pentanoic acid, for which the name eremorigidane E is suggested. ^{1}H and ^{13}C NMR data are provided in Table 2, and ^{1}H NMR, ^{13}C NMR, HSQC, HMBC, COSY, and

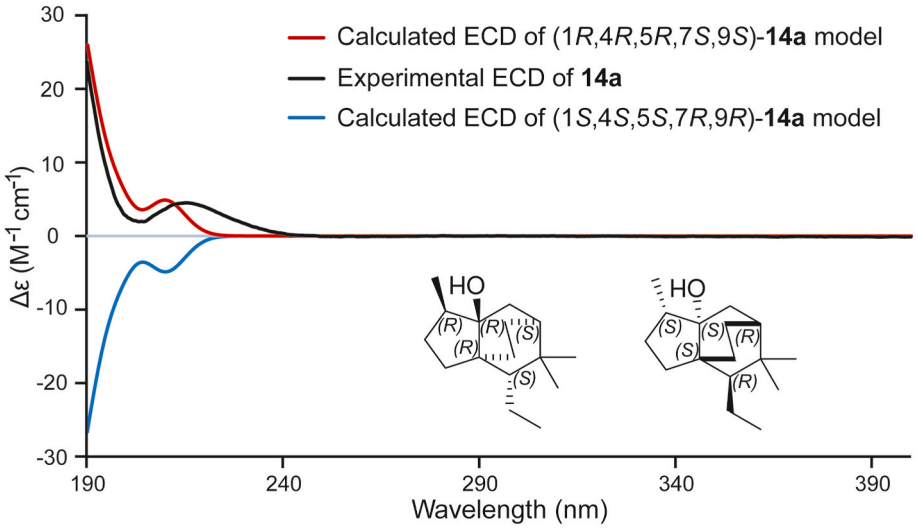

Fig. 5. Comparison of the experimental ECD spectrum of **14a** and calculated ECD spectra of an enantiomeric pair of model compounds of **14a** with a truncated side chain.

ROESY spectra are provided in Supplementary data Figs. S35–S40.

The material eluted with peak *9* was assigned the molecular formula $C_{20}H_{32}O_3$ on the basis of an $[M-H]^-$ ion observed at *m/z* 319.2268 (calcd for $C_{20}H_{31}O_3^-$ 319.2279, ΔM +3.3 ppm) in the HRMS spectrum (Supplementary data Fig. S8), which corresponds to five indices of hydrogen deficiency. The 1D and 2D NMR spectra of **9** suggested the eremane scaffold as also found in **2**, **14a**, and **14b** as the core structure of this diterpenoid, and comparison of NMR data of **9** and **14a** showed these two compounds to have the same side chain (C-15 to C-20). However, a few remarkable differences of their NMR spectra indicated that the structure for the tricyclo [5.2.2.0^{1,5}] undecane ring system of **9** and **14a** are differing slightly. Thus, the absence of the H_3-12 methyl singlet seen in **14a** and the appearance of a pair of olefinic methylene protons (δ_H 4.82, 1H, br d, J = 1.8 Hz, H-12a and δ_H 4.88, 1H, br d, J = 1.8 Hz, H-12b) in the spectra of **9**, suggested a $\Delta^{4,12}$ double bond in **9**. Another difference was the absence of the oxygenated quaternary C-5 seen in **14a** and the presence of a methine proton at δ_H 2.20 (1H, overlap, H-5, $\delta_{C\text{-}5}$ 48.8) in the spectra of **9**. Finally, only one methyl singlet (δ_H 1.04, 3H, s, H_3-13) was observed in the ^{1}H NMR spectrum of **9** compared to two methyl singlets in the spectra of **14a**. Instead, an oxymethylene group (δ_H 3.28, 1H, d, J = 10.8 Hz, H-14a and δ_H 3.47, 1H, d, J = 10.8 Hz, H-14b) appeared in the spectra of **9**, and HMBC correlations from H-14a and H-14b to C-7, C-8 and C-9 confirmed the position of the oxymethylene group (Fig. 3).

The ROESY spectrum of **9** showed correlations between H-5 and H-9, H-14b and H-6β, H-14b and H-9 (Supplementary data Fig. S28), which indicated these protons to be β-oriented. In addition, the ROE correlation between H-15a and H-11α and H_3-13 assigned their α configuration. The relative configuration of **9** was thus established as shown in Fig. 4. The absolute configuration of **9** was determined by comparison of calculated and experimental ECD data. Similar to **14a**, the ECD calculation of **9** was performed using a model compound (Fig. 6) representing the tricyclo [5.2.2.0^{1,5}] undecane ring skeleton with a truncated side chain. Conformational searches for the 3D structure of (1*S*,5*S*,7*S*,8*R*,9*R*)-**9 model** and (1*R*,5*R*,7*R*,8*S*,9*S*)-**9 model** yielded 13 and 15 possible conformers, respectively, among which eight and ten dominant conformers that were used for calculation of the final theoretical ECD spectra (Supplementary data Tables S6–S9). The results are shown in Fig. 6, and the experimental ECD spectrum of **9**, shows one single strong negative Cotton effect around 200 nm, as also seen in the calculated ECD spectrum of (1*S*,5*S*,7*S*,8*R*,9*R*)-**9 model** with a similarity index Δ_{ESI} of 0.9852. This unambiguously established the configuration of **9** to be 1*S*,5*S*,7*S*,8*R*,9*R*, with C-18 tentatively assigned the *R*-configuration based on biosynthetic arguments. Thus, the structure of **9** was established to be (*R*)-5-((3a*S*,4*R*,5*R*,6*S*,7a*S*)-5-(hydroxymethyl)-5-methyl-1-methyleneoctahydro-3a,6-ethanoinden-4-yl)-2-methylpentanoic acid, for which the name eremorigidane C is suggested. ^{1}H and ^{13}C NMR data are provided in Table 3, and ^{1}H NMR, HSQC, HMBC, COSY, and ROESY spectra are provided in Supplementary data Figs. S24–S28.

The material eluted with peak *14c* was assigned the molecular formula $C_{20}H_{32}O_2$ on the basis of an $[M-H]^-$ ion observed at *m/z* 303.2341 (calcd for $C_{20}H_{31}O_2^-$ 303.2329, ΔM −3.8 ppm) in the HRMS spectrum (Supplementary data Fig. S11), which corresponds to five indices of hydrogen deficiency. The COSY spectrum of **14c** (Supplementary data Fig. S45) revealed the H_2-2↔H_2-3↔H-4↔H_3-12 spin system for the A-ring and the H_2-15↔H_2-16↔H_2-17↔H-18↔H_3-19 spin system for the side chain, as also observed for **14a**. However, the remaining core structure was found to be a ring system consisting of a fused five-membered and six-membered ring (Fig. 2). Thus, the COSY spectrum revealed the H_2-6↔H-7↔H_2-10↔H_2-11 spin system and together with HMBC correlations from H_2-6 and H-7 to C-5, from H_3-13/H_3-14 to C-7, C-8, and C-9, from H_2-2 to C-1, C-5, and C-9, and from H_2-11 to C-1 and C-5 (Fig. 3). The core tricyclic structure in **14c** was thus established as a tricyclo[6.2.1.0^{1,5}] undecane ring, corresponding to the isozizaene skeleton (Hong and Tantillo, 2014). The zizaene/isozizaene skeleton has previously been found in sesquiterpenoids isolated from *E. georgei* (Carrol et al., 1976), but this is the first report on an isozizaene-type diterpenoid.

ROE correlations between H-4 and H-6α, as well as between H-6α and H_3-13 suggested these to be α-oriented, while ROE correlations between H_3-12 and H-10α and between H-10α and H-7 and H_3-14 indicated H_3-12, H_2-10, H_2-11, and H_3-14 to be β-oriented (Fig. 4). The flexibility of the side chain at C-9 prevented assignment of the relative stereochemistry of C-18 by ROE correlations. Thus, to determine the absolute configuration of the core isozizaene skeleton as well as of C-18, quantum chemical calculations of ECD spectra were performed for the entire structure of **14c** – without the truncations used for the model compounds of **9** and **14a** above. Based on biosynthetic arguments, the 4*R*,5*S*,7*R*,18*R* is the most likely, and thus both (4*R*,5*S*,7*R*,18*R*)-**14c** and its enantiomer (4*S*,5*R*,7*S*,18*S*)-**14c** were subjected to ECD calculations. Conformational searches for (4*R*,5*S*,7*R*,18*R*)-**14c** and (4*S*,5*R*,7*S*,18*S*)-**14c** resulted in 92 and 87 possible conformers, respectively. After geometry optimization, 23 and 22 dominant conformers with Boltzmann populations above 1% were chosen and used for calculation of ECD spectra of this pair of enantiomers (Supplementary data

Table 2
^{1}H NMR (600 MHz) and ^{13}C NMR (150 MHz) spectroscopic data of compounds **2**, **14a**, and **14b** (δ in ppm, J in Hz).

No.	2[d]		14a[e]		14b[e]	
	δ_C, type	δ_H, mult (J)[b]	δ_C, type	δ_H, mult (J)[b]	δ_C, type[a]	δ_H, mult (J)[b]
1	55.3, C		48.8, C		51.2, C	
2	33.9, CH_2	α: 1.65, dd (15.2, 2.0) β: 2.11, dd (15.2, 4.0)	31.5, CH_2	α: 1.16, overlap[c] β: 1.44, overlap[c]	32.9, CH_2	α: 1.41, overlap[c] β: 1.48, overlap[c]
3	29.7, CH_2	α: 1.35, overlap[c] β: 1.86, ddd (10.0, 7.8, 3.8)	29.1, CH_2	α: 1.22, ddd (11.4, 7.4, 3.8) β: 1.79, overlap[c]	36.3, CH_2	2.19, overlap[c]
4	42.7, CH	1.91, qdd (7.8, 2.4, 1.0)	41.4, CH	1.95, qdd (7.0, 2.4, 1.0)	125.7, C	
5	81.3, C		82.3, C		140.5, C	
6	31.4, CH_2	α: 1.34, overlap[c] β: 1.63, overlap[c]	37.3, CH_2	α: 1.42, overlap[c] β: 1.81, overlap[c]	25.2, CH_2	α: 1.16, overlap[c] β: 1.51, overlap[c]
7	44.4, CH	2.22, br dt (10.0, 2.4)	41.3, CH	1.13, overlap[c]	40.8, CH	1.23, overlap[c]
8	35.3, C		34.1, C		34.8, C	
9	60.8, CH	1.79, br t (2.8)	43.9, CH	1.78, overlap[c]	52.1, CH	1.08, overlap[c]
10	28.8, CH_2	α: 1.21, dt (13.2, 3.2) β: 1.41, overlap[c]	23.7, CH_2	α: 1.12, overlap[c] β: 1.75, overlap[c]	24.3, CH_2	α: 1.23, overlap[c] β: 1.79, overlap[c]
11	30.1, CH_2	α: 1.35, overlap[c] β: 1.48, overlap[c]	23.0, CH_2	α: 1.13, overlap[c] β: 1.38, overlap[c]	23.1, CH_2	α: 1.16, overlap[c] β: 1.40, overlap[c]
12	13.0, CH_3	0.95, d (6.5)	12.8, CH_3	0.93, d (6.8)	13.7, CH_3	1.56, s
13	30.4, CH_3	1.26, s	32.2, CH_3	1.07, s	32.6, CH_3	0.99, s
14	26.4, CH_3	0.88, s	24.9, CH_3	0.95, s	24.7, CH_3	0.98, s
15	41.9, CH_2	a: 2.00, dd (19.6, 2.0) b: 2.10, br d (19.6)	28.9, CH_2	a: 1.29, ddd (12.0, 9.6, 4.8) b: 1.41, overlap[c]	27.5, CH_2	a: 1.23, overlap[c] b: 1.45, overlap[c]
16	219.8, C		27.9, CH_2	a: 1.06, overlap[c] b: 1.44, overlap[c]	28.9, CH_2	a: 1.25, overlap[c] b: 1.46, overlap[c]
17	35.3, CH_2	a: 1.47, overlap[c] b: 1.62, overlap[c]	34.2, CH_2	a: 1.41, overlap[c] b: 1.63, m	34.2, CH_2	a: 1.46, overlap[c] b: 1.69, m
18	40.8, CH	2.41, tq (7.0, 6.6)	39.4, CH	2.41, tq (7.0, 6.6)	39.4, CH	2.46, overlap[c]
19	17.7, CH_3	1.14, d (7.0)	16.9, CH_3	1.14, d (7.0)	17.0, CH_3	1.18, d (7.0)
20	180.9, C		182.9, C		183.1, C	

[a] ^{13}C NMR data assigned by HSQC and HMBC experiments.
[b] Multiplicities reported as apparent splittings: s = singlet, d = doublet, t = triplet, q = quartet, m = multiplet, br = broad.
[c] Multiplicities undetermined due to overlapping signals.
[d] NMR data acquired in methanol-d_4.
[e] NMR data acquired in chloroform-d.

Tables S14–S17). The results are shown in Fig. 7, and the experimental ECD spectrum significantly corresponded to that of the calculated spectrum of (4*R*,5*S*,7*R*,18*R*)-**14c** with a similarity index Δ_{ESI} of 0.9278 (Fig. 7). The large positive Cotton effect around 225 nm is mainly attributed to the isozizaene skeleton, so to ascertain the correct configuration of C-18, the ECD spectrum of the 18-epimeric (4*R*,5*S*,7*R*,18*S*)-**14c** was calculated. Thus, 89 possible conformers were obtained for (4*R*,5*S*,7*R*,18*S*)-**14c**, among which 23 conformers with a Boltzmann population higher than 1% (Supplementary data Tables S18 and S19) were used for calculation of the ECD spectrum. The result is shown in Supplementary data Fig. S48, and the differences between the experimental ECD spectrum of **14c** and the calculated spectrum for (4*R*,5*S*,7*R*,18*S*)-**14c** (similarity index Δ_{ESI} of 0.7635) thus confirms **14c** to have the 4*R*,5*S*,7*R*,18*R* configuration. Thus, the structure of **14c** was established to be (*R*)-2-methyl-5-((3*R*,3a*S*,6*R*)-3,7,7-trimethyl-2,3,4,5,6,7-hexahydro-1*H*-3a,6-methanoazulen-8-yl)pentanoic acid, for which the name eremorigidane F is suggested. ^{1}H and ^{13}C NMR data are provided in Table 3, and ^{1}H NMR, ^{13}C NMR, HSQC, HMBC, COSY, and ROESY spectra are provided in Supplementary data Figs. S41–S46.

The material eluted with peak *7a* was assigned the molecular formula $C_{20}H_{32}O_4$ on the basis of an $[M-H]^-$ ion observed at *m/z* 335.2233 (calcd for $C_{20}H_{31}O_4^-$ 335.2228, ΔM −1.5 ppm) in the HRMS spectrum (Supplementary data Fig. S7), which corresponds to five indices of hydrogen deficiency. Intensive analysis of ^{1}H NMR and 2D homo- and heteronuclear NMR data revealed **7a** to be a previously undescribed viscidane type diterpenoid, whose framework is featured by a spiro [4,5] decane ring system comprising ring A (five-membered ring) and ring B (six-membered ring) as shown in Fig. 2. The structure of ring A in conjunction with the linear side chain was established by the H-7↔H_2-8↔H_2-9↔H-10↔H-11(H_3-18)↔H_2-12↔H_2-13↔H-14↔H_3-16/H_3-17 spin system, the latter being long-range couplings, observed in the COSY spectrum (Supplementary data Fig. S22). HMBC correlations from H-7 and H_2-8 to the quaternary carbon at δ_C 179.9 confirmed the carboxylic acid at C-7 on ring A (Fig. 3). The structure of ring B was established based on the H_2-2↔H-3↔H_2-19 spin system, the latter via long-range couplings, and the H-5↔H_2-6 spin system, as well as HMBC correlations from oxymethylene H_2-19 to C-3, C-4 and C-5, and from H-3 to C-5 (Fig. 3). Finally, the position of the side chain and the spiro junction between ring A and ring B were established on the basis of HMBC correlations from H-7 to C-1 and C-2, from H_2-6 to C-1 and C-10, and from H-3 to C-1 (Fig. 3).

The relative stereochemistry of **7a** was determined by analysis of the ROESY spectrum. As shown in Fig. 4, key ROE correlations were detected between H-7 and H-2α and H-11, indicating these to be positioned α. Likewise, ROE correlations between H-10 and H_2-6 indicated these to be oriented β. As for the eremane and isozizaene diterpenoids identified in this study, comparison of experimental and theoretical ECD spectra was used to determine the absolute stereochemistry of the viscidane diterpenoid **7a**. To reduce considerably the computational cost, truncation of the 2-methylprop-1-ene moiety from C-14 to C-17 resulted in the model compound of **7a**. For determination of the absolute stereochemistry, conformational searches were performed for the enantiomeric pair of model compounds with a truncated side chain, i.e., (1*S*,5*R*,7*R*,10*S*,11*S*)-**7a model** and (1*R*,5*S*,7*S*,10*R*,11*R*)-**7a model**. The experimental ECD spectrum of **7a** and the calculated ECD data of the (1*S*,5*R*,7*R*,10*S*,11*S*)-**7a model** (Fig. 8) matched well with a similarity index Δ_{ESI} of 0.9064, confirming the 1*S*,5*R*,7*R*,10*S*,11*S* configuration of **7a**. Thus, the structure of **7a** was established as (1*R*,4*S*,5*S*,9*R*)-9-hydroxy-8-(hydroxymethyl)-4-((*S*)-6-methylhept-5-en-2-yl)spiro[4.5]dec-7-ene-1-carboxylic acid, for which the name eremorigidane B is suggested. ^{1}H and ^{13}C NMR data are provided in Table 3, and ^{1}H NMR, HSQC, HMBC, COSY, and ROESY spectra are provided in Supplementary data Figs. S19–S23.

Although not as frequently found in *Eremophila* as serrulatane diterpenoids, previous studies have reported the isolation of eremane (Croft et al., 1984; Carroll et al., 1985; Ghisalberti et al., 1990) and viscidane (Forster et al., 1986, 1993; Syah et al., 1997; Tahtah et al., 2016; Biva et al., 2019; Zhao et al., 2023) diterpenoids in *Eremophila*. Few of these viscidane diterpenoids show antibacterial (Biva et al., 2019) and PTP1B inhibitory activity (Tahtah et al., 2016). PTP1B

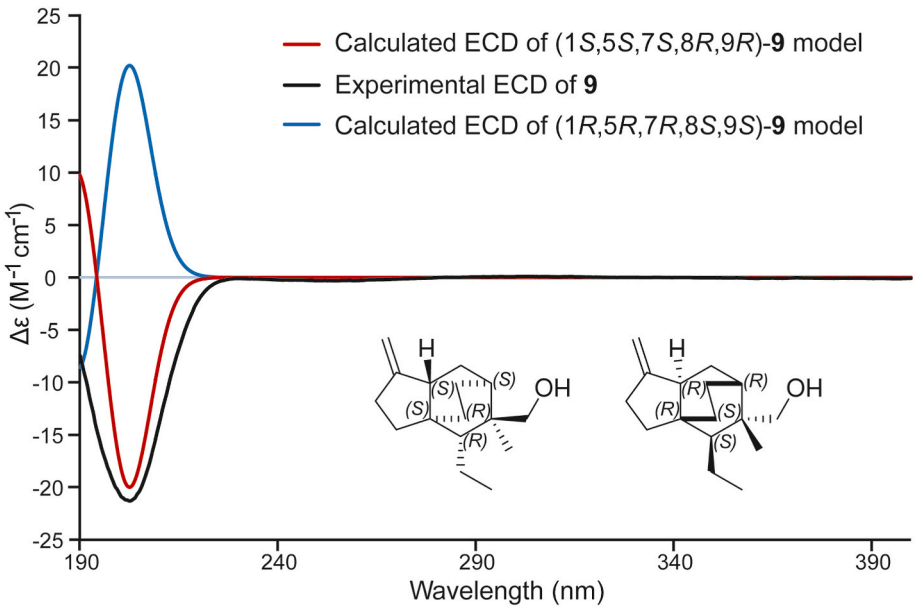

Fig. 6. Comparison of the experimental ECD spectrum of **9** and calculated ECD spectra of an enantiomeric pair of model compounds of **9** with a truncated side chain.

inhibitory activity has however never been reported for any eremane diterpenoids before.

2.4. Plausible enzymatic steps involved in eremane and isozizaene biosynthesis

The abundant structural diversity of diterpenoids present in the *Eremophila* genus in combination with discovered interesting bioactivities, renders biological production of selected diterpenoids in heterologous hosts relevant (Gericke et al., 2020, 2021; Hansen et al., 2022). A prerequisite for this to happen is elucidation of their route of biosynthesis. Experimental studies in *E. lucida*, *E. drummondii* and *E. denticulata* demonstrated that (*Z*,*Z*,*Z*)-nerylneryl diphosphate (NNDP) is the non-canonical terpene precursor of polycyclic diterpenes with serrulatane, viscidane, and cembrane skeletons (Gericke et al., 2020). Likewise, biosynthesis of acyclic diterpenes from *E. glutinosa* and *E. exilifolia* has been proposed to originate from NNDP (Ghisalberti et al., 1981). In contrast, based on the *E*-configuration of the double bonds present, the pathway for decipiene diterpenoids in *Eremophila clarkei* was concluded to proceed from the canonical precursor (*E*,*E*,*E*)-geranylgeranyl diphosphate (Ghisalberti, 1995; Liang et al., 2023b) and involving a cationic intermediate equivalent to the bisabolyl cation, which has been demonstrated to serve as a hub for biosynthesis of an array of diverse and structurally complex sesquiterpenoids such as bisabolene, acoradiene, curcumene, cedrene, zizaene and isozizaene (Hong and Tantillo, 2014).

The biosynthesis of eremane and isozizaene diterpenoids therefore probably also includes the bisabolyl-type diterpenoid cation as an intermediate, and (*E*,*E*,*E*)-geranylgeranyl diphosphate (GGDP) as the corresponding C_{20} precursor (Liang et al., 2023b). As shown in Fig. 9, a [1,2]-hydride migration within the bisabolyl-type diterpenoid cation produces intermediate **A**, which following a 6,10-cyclization to yield a 6*R*- or 6*S* acorenyl-type diterpenoid cation ($\mathbf{B_1}$ or $\mathbf{B_2}$) (Eaton and Christianson, 2023). Afterwards, a series of cyclization, alkyl and methyl shift reactions and a deprotonation occur in sequence from the 6*S* acorenyl-type diterpenoid cation ($\mathbf{B_1}$) to generate the core structure of (+)-isozizaene diterpenoid. Similar sequential reactions from the 6*R* acorenyl-type diterpenoid cation ($\mathbf{B_2}$) form the carbocation intermediate $\mathbf{E_2}$ which by a subsequent [1,2]-hydride migration, an alkyl shift reaction, and a deprotonation, affords the main scaffold of the eremane diterpene. None of the diterpenoid synthases involved in biosynthesis of the basic skeleton of (+)-isozizaene and eremane diterpenoids have been identified to date, but the proposed biosynthetic scheme is in agreement with the known ability of diterpene synthases to catalyze a carbocation-based cascade of cyclization reactions involving hydride migrations, methyl shifts, and Wagner-Meerwein rearrangements to afford structurally complex diterpene carbon scaffolds. To decipher the specific cyclization cascade, isotopic labelling experiments, homology modelling and site-directed mutagenesis are required to identify the presence of the critical amino acid residues that would favor the suggested unique carbocation-driven cascade cyclization mechanism (Li et al., 2023). The *epi*-isozizaene sesquiterpene synthase from the bacterium *Streptomyces coelicolor* has been isolated and crystallized. The active site was shown to possess a product-shaped contour chaperoning the conformations of the flexible farnesyl diphosphate substrate and the cascade of multiple carbocation intermediates preceding the formation of *epi*-isozizaene. Single amino acid mutations were demonstrated to remold the contour of the active site and redirect the cyclization cascade towards formation of other sesquiterpenes and different stereoisomers of the acorenyl sesquiterpenoid cation (Eaton and Christianson, 2023). In a similar manner, we envision that the active site of the *E. rigida* diterpene synthase involved in eremane and (+)-isozizaene synthesis is not framed to secure formation of a single stereoisomer of the acorenyl diterpenoid cation (Fig. 9). Other routes to formation of the two classes of diterpenoids are possible. Such alternative routes could result in different origins of some of the carbon atoms in the diterpenes formed (Hong and Tantillo, 2018). Discrimination between these will depend on identification and structural knowledge of the diterpenoid synthase involved and predictions on their ability to accommodate the different carbocation intermediates within the product-shaped contour of its active site.

2.5. The preliminary structure-activity relationship (SAR) of isolated compounds

The PTP1B inhibitory activities of all metabolites isolated from acetonitrile extract of *E. rigida* were firstly evaluated at a concentration of 100 μM (Table 4). The isolated eremane, viscidane, and isozizaene diterpenoids, i.e., **2**, **7a**, **9**, **14a**, **14b**, and **14c** showed less than 50% inhibition at this concentration. However, a series of highly methoxylated flavonoids and triterpenoids, i.e., **1**, **3**, **15**, **16**, and **17** showed more than 50% inhibition at 100 μM, and two-fold dilution series for assessment of their dose-dependent effects were prepared. The results

Table 3
^{1}H NMR (600 MHz) and ^{13}C NMR (150 MHz) spectroscopic data of compounds **7a**, **9**, and **14c** (δ in ppm, J in Hz).

No.	7a[d]		9[e]		14c[e]	
	δ_C, type[a]	δ_H, mult (J)[b]	δ_C, type[a]	δ_H, mult (J)[b]	δ_C, type	δ_H, mult (J)[b]
1	50.0, C		44.5, C		143.6, C	
2	30.6, CH_2	α: 1.80, br dd (17.3, 5.2) β: 2.18, br dt (17.3, 2.2)	32.8, CH_2	α: 1.07, br dd (12.6, 3.4) β: 1.77, overlap[c]	26.6, CH_2	α: 2.13, ddd (12.4, 8.4, 3.8) β: 2.21, q (6.9)
3	123.5, CH	5.72, br dd (3.3, 1.4)	30.5, CH_2	α: 2.19, overlap[c] β: 2.40, dt (10.0, 8.0)	32.3, CH_2	α: 1.30, overlap[c] β: 1.81, overlap[c]
4	140.7, C		156.1, C		40.3, CH	1.89, qdd (7.0, 3.4, 1.0)
5	66.8, CH	4.55, br t (7.8)	48.8, CH	2.20, overlap[c]	53.9, C	
6	41.4, CH_2	α: 1.90, overlap[c] β: 1.95, overlap[c]	27.0, CH_2	1.71, dd (9.2, 2.8)	39.0, CH_2	α: 1.31, overlap[c] β: 1.56, overlap[c]
7	52.7, CH	2.71, dd (8.4, 2.4)	32.4, CH	1.56, br s	48.2, CH	1.82, overlap[c]
8	26.5, CH_2	α: 1.76, overlap[c] β: 1.92, overlap[c]	39.8, C		41.1, C	
9	27.9, CH_2	α: 1.52, overlap[c] β: 2.03, overlap[c]	38.8, CH	0.72, br s	132.6, C	
10	52.7, CH	2.06, overlap[c]	23.1, CH_2	α: 1.44, overlap[c] β: 1.75, overlap[c]	34.6, CH_2	α: 1.30, overlap[c] β: 1.64, br dt (10.6, 2.0)
11	33.9, CH	1.52, overlap[c]	28.3, CH_2	α: 1.12, br t (12.0) β: 1.80, br dd (12.0, 4.8)	25.0, CH_2	α: 1.59, overlap[c] β: 1.74, overlap[c]
12	36.7, CH_2	a: 1.11, ddd (13.6, 9.6, 4.8) b: 1.48, dt (9.6, 2.8)	104.6, CH_2	a: 4.82, br d (1.8) b: 4.88, br d (1.8)	17.4, CH_3	0.83, d (7.0)
13	26.0, CH_2	a: 1.93, overlap[c] b: 2.06, overlap[c]	19.6, CH_3	1.04, s	29.6, CH_3	0.99, s
14	125.6, CH	5.10, t sep (7.2, 1.4)	70.9, CH_2	a: 3.28, d (10.8) b: 3.47, d (10.8)	25.5, CH_3	0.97, s
15	131.9, C		25.9, CH_2	a: 1.25, overlap[c] b: 1.40, overlap[c]	28.9, CH_2	1.84, overlap[c]
16	25.6, CH_3	1.67, s	28.8, CH_2	a: 1.22, overlap[c] b: 1.34, overlap[c]	27.6, CH_2	1.38, overlap[c]
17	17.4, CH_3	1.61, s	34.3, CH_2	a: 1.42, overlap[c] b: 1.65, m	34.4, CH_2	a: 1.42, overlap[c] b: 1.67, overlap[c]
18	20.3, CH_3	1.00, d (6.7)	39.2, CH	2.46, tq (7.0, 6.6)	39.1, CH	2.48, tq (7.0, 6.6)
19	63.8, CH_2	a: 4.11, d (13.2) b: 4.20, d (13.2)	17.1, CH_3	1.17, d (7.0)	17.1, CH_3	1.19, d (7.0)
20	179.9, C		181.5, C		181.3, C	

[a] ^{13}C NMR data assigned by HSQC and HMBC experiments.
[b] Multiplicities reported as apparent splittings: s = singlet, d = doublet, t = triplet, q = quartet, sep = septet, m = multiplet, br = broad.
[c] Multiplicities undetermined due to overlapping signals.
[d] NMR data acquired in methanol-d_4.
[e] NMR data acquired in chloroform-*d*.

expressed as IC_{50} values are listed in Table 4, with corresponding dose-dependent curves provided in Supplementary data Fig. S49.

Among the isolated *O*-methylated flavonoids, penduletin (**3**) exhibited the strongest PTP1B inhibitory activity with an IC_{50} value of 18.3 ± 1.5 μM. The *in vitro* antidiabetic potential of penduletin has previously been demonstrated on the basis of its α-glucosidase (Hu et al., 2017) and α-amylase (Al-Dabbas et al., 2006) inhibitory activities, but this is the first report on the PTP1B inhibitory activity of penduletin. As seen in Table 4, other *O*-methylated flavonoids exhibited weaker PTP1B inhibitory activity than **3**, suggesting that a hydroxy group at C-4′ and preferably a high number of methoxy substituents at C-3, C-5, C-6 and/or C-7 is needed for strong PTP1B inhibitory activity.

All identified triterpenoids showed PTP1B inhibitory activity with IC_{50} values in a range from 6.3 ± 0.3 μM to 55.7 ± 5.5 μM. 3-Oxo-oleanolic acid (**17**) was the most potent PTP1B inhibitor (IC_{50} = 6.3 ± 0.3 μM) with an IC_{50} value two fold lower than that of the positive control RK-682 (IC_{50} = 13.7 ± 1.3 μM), indicating the potential of 3-oxo-oleanolic acid as a promising PTP1B inhibitor needing further investigations. As shown in Table 4, the IC_{50} value of **16** was about 1.5-fold higher than **17**, which suggests that the ketone at C-3 is important for the PTP1B inhibitory activity. Compound **15**, a ring-opened analogue of **17**, showed dramatically weaker inhibition than **17**, indicating that the intact ring skeleton of pentacyclic triterpenoids is crucial for PTP1B inhibitory activity of this class of natural products. Surprisingly, **14a**-**14c** did only show weak inhibitory activity at 100 μM despite the strong inhibitory activity correlated with peak *14* (Fig. 1). This may be due to the very high amount of material eluted with peak *14* (see Section 4.5), that the compounds eluted with peak *14* act synergistically, or that an additional high-activity inhibitor was not isolated. Likewise, the lack of inhibitory activity correlated with HPLC peaks *3* and *16* in the biochromatogram, despite isolated **3** and **16** showing strong inhibitory activity, may be due to very low concentration of the material eluted with these two peaks. This underpins the importance of being aware that the inhibition peaks in the biochromatogram are relative and thus strongly affected by the amount and the nature of the material eluted with each peak.

3. Conclusions

In conclusion, high-resolution inhibition profiling combined with HPLC-PDA-HRMS, semi-preparative- and analytical-scale HPLC separations and NMR spectroscopy were used to investigate an PTP1B-inhibiting acetonitrile extract from the leaves of *E. rigida*, leading to isolation and identification of six previously undescribed diterpenoids, including one isozizaene, one viscidane, and four eremane type diterpenoids, together with six known *O*-methylated flavonoids and three known triterpenoids. One of the flavonoids and all three triterpenoids showed moderate to strong PTP1B inhibitory activity. This study for the first time investigated and reported chemical constituents and bioactivities of *E. rigida*. The findings in the present study expand chemical

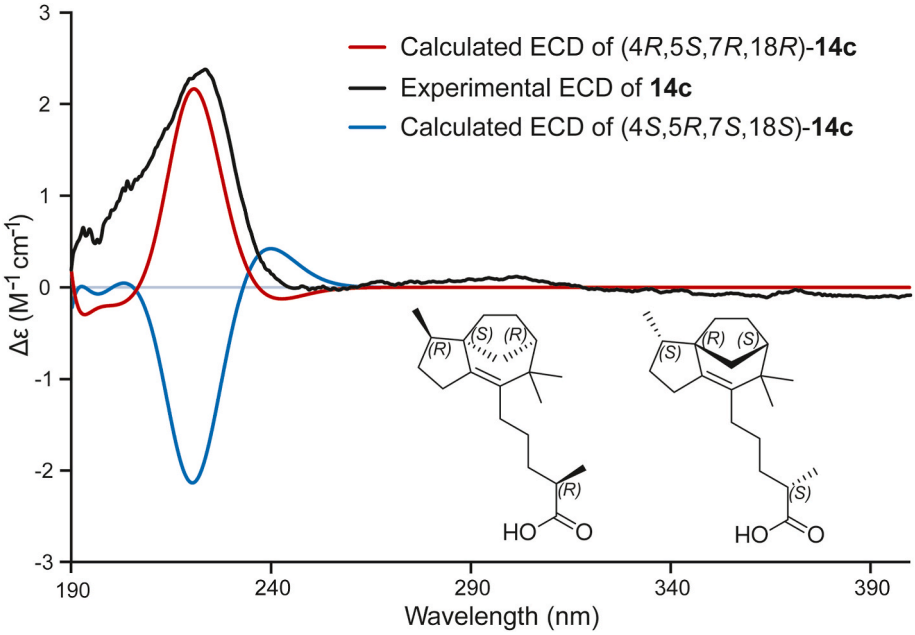

Fig. 7. Comparison of the experimental ECD spectrum of **14c** and calculated ECD spectra of an enantiomeric pair of **14c**.

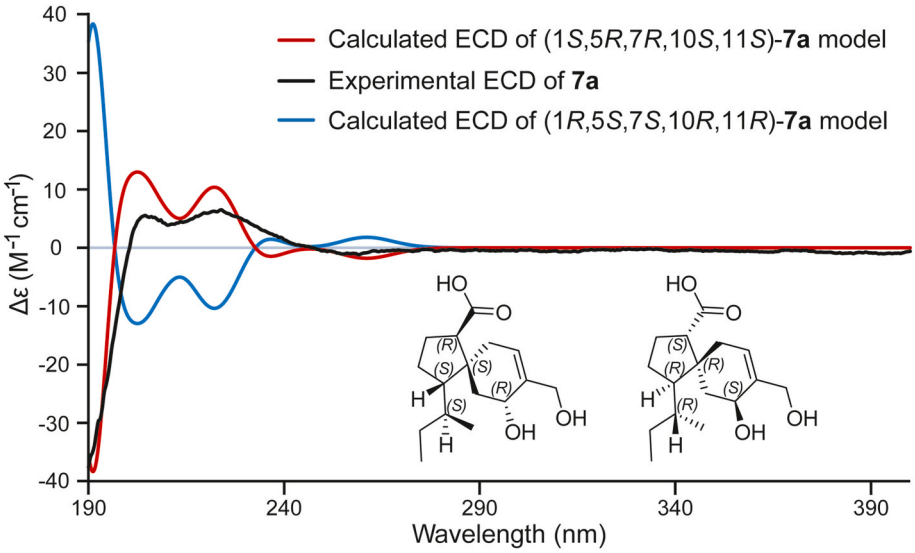

Fig. 8. Comparison of the experimental ECD spectrum of **7a** and calculated ECD spectra of an enantiomeric pair of model compounds of **7a** with a truncated side chain.

diversity of structurally unique eremane, viscidane and isozizaene diterpenoids from the genus *Eremophila* and supports that *Eremophila.* spp are valuable sources in the search for PTP1B inhibitors.

4. Experimental

4.1. Chemicals

$NaH_2PO_4{\cdot}2H_2O$, NaOH, NaN_3, NaCl, Na_2HPO_4, acetic acid, phosphoric acid, 2-chloro-4-nitrophenyl-α-D-maltotrioside (CNP-G3), dimethyl sulfoxide (DMSO), dithiothreitol (DTT), *N,N,N′,N′*-ethylenediaminetetraacetate (EDTA), *p*-nitrophenyl α-D-glucopyranoside (*p*-NPG), *p*-nitrophenyl phosphate (*p*-NPP), tris(hydroxymethyl)-aminomethane (Tris), bis(2-hydroxyethyl)-imino-tris(hydroxymethylmethane) (Bis-Tris), α-glucosidase type I (EC 3.2.1.20, from *Saccharomyces cerevisiae*, lyophilized powder) and α-amylase type VI-B (E.C. 3.2.1.1, from porcine pancreas, lyophilized powder) were purchased from Sigma-Aldrich (St. Louis, MO, USA), recombinant human protein tyrosine phosphatase 1B (PTP1B) (BML-SE332-0050, EC 3.1.3.48) and RK-682 from Enzo Life Sciences (Farmingdale, NY, USA), and formic acid and calcium acetate from Merck (Darmstadt, Germany). HPLC-grade acetonitrile was purchased from VWR International (Søborg, Denmark), and methanol-d_4 and chloroform-*d* from Euriso-top (Saint-Aubin Cesex, France). Deionization and filtration of water was conducted through a 0.22-μm membrane on a Milli-Q Plus system (Millipore, Billerica, MA, USA).

4.2. Plant material and extraction

Leaves of *Eremophila rigida* Chinnock were collected 74.3 km south of Capricorn Roadhouse, Western Australia (24 4 55.7 S, 119 42 50.5 E) and identified by Dr Bevan Buirchell. A voucher specimen has been deposited at the University of Melbourne Herbarium, Melbourne,

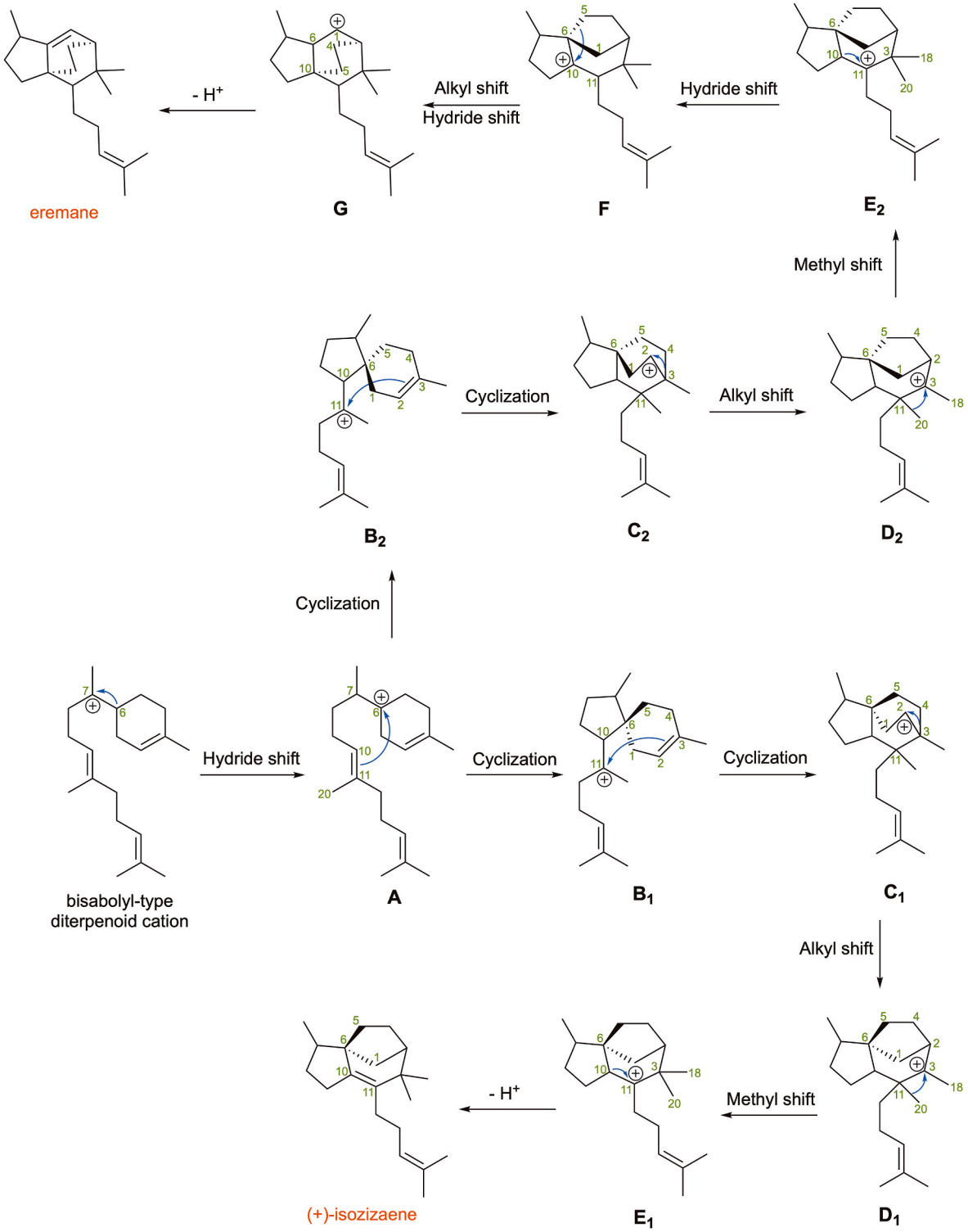

Fig. 9. Plausible biosynthetic route for formation of the eremane and isozizaene core skeletons.

Victoria, Australia (accession number MELUD127845a). To extract leaf resins, leaf material (78.6 g) was submerged in 250 mL of acetonitrile and shaken for 10 min (Ratek, Knox City, Victoria, Australia). The extract was filtered using a glass funnel and dried *in vacuo* at 40 °C using a rotary evaporator (IKA RV10). The dry extract (3.36 g) was transferred to amber-colored vials using a small volume of methanol and dried under nitrogen gas, then stored at −20 °C. Samples for HPLC, bioassays and NMR were prepared by redissolving this dried material to the concentrations mentioned for each analysis.

4.3. α-Glucosidase, α-amylase and PTP1B inhibition assays

The α-glucosidase inhibition assay was performed in 96-well microplates as previously reported (Liang et al., 2021). In short, individual samples for each well were dissolved in 10 μL DMSO and supplemented with 90 μL buffer and 80 μL α-glucosidase enzyme solution (2.0 U/mL in buffer) to a total volume of 200 μL. The buffer (100 mM, pH 7.5) contains 34 mM $NaH_2PO_4{\cdot}2H_2O$, 66 mM Na_2HPO_4 and 0.02% NaN_3. The microplate samples were then incubated at 28 °C for 10 min

Table 4
PTP1B inhibitory activity of isolated compounds at 100 μM and IC_{50} values for the compounds showing more than 50% inhibition at this concentration.

Compound	PTP1B inhibition	
	Percentage at 100 μM[a,b]	IC_{50} (μM)[a,b]
1	62.3 ± 2.6	>100
2	−6.6 ± 2.8	n.d.
3	103.7 ± 6.0	18.3 ± 1.5
4	14.3 ± 1.0	n.d.
6	20.5 ± 1.4	n.d.
7a	0.4 ± 6.6	n.d.
7b	4.5 ± 4.8	n.d.
9	34.7 ± 6.1	n.d.
10	−0.5 ± 1.2	n.d.
14a	10.8 ± 4.5	n.d.
14b	28.5 ± 6.4	n.d.
14c	20.4 ± 2.7	n.d.
15	99.6 ± 2.6	55.7 ± 5.5
16	100.1 ± 6.0	9.9 ± 0.5
17	100.9 ± 10.9	6.3 ± 0.3
RK-682[c]	n.d.	13.7 ± 1.3

[a] Results expressed as mean ± standard error of three independent experiments.
[b] n.d.: not determined.
[c] Reference compound.

followed by addition of 20 μL *p*-NPG solution (10 mM in buffer) to each well to initiate the enzymatic reaction after well mixing. The absorbance of the formed cleavage product, the strongly chromogenic *p*-nitrophenolate ion produced in each well, was recorded every 30 s for 35 min at 405 nm, which yielded enzyme activity (ΔAU/s). A Thermo Scientific Multiskan FC microplate photometer (Thermo Scientific, Waltham, MA, USA) equipped with a built-in incubator was used for enzyme incubation and measurement of absorbance, which was controlled by a coupled SkanIt ver. 2.5.1 software. DMSO was included as blank sample and all measurements were performed in triplicate. The α-glucosidase inhibition was calculated according to the equation below:

$$\text{Percent inhibition} = \frac{Slope(blank) - Slope(sample)}{Slope(blank)} \times 100\% \quad \text{(Eq. 1)}$$

The α-amylase inhibition assay was performed with a procedure similar to the above-mentioned α-glucosidase inhibition assay as previously described (Zhao et al., 2018). Briefly, the sample for each well was dissolved in 20 μL DMSO and supplemented with 80 μL buffer and 80 μL α-amylase enzyme solution (2.0 U/mL in buffer). The buffer (110 mM, pH 6.0) contains $NaH_2PO_4{\cdot}2H_2O$, Na_2HPO_4, 60 mM NaCl and 0.02% NaN_3. The microplate samples were then incubated at 37 °C for 10 min followed by addition of 20 μL CNP-G3 solution (10 mM in buffer) to each well to initiate the enzymatic reaction after well mixing. The absorbance of the cleavage product formed in each well was measured every 3 min for 30 min at 405 nm on the same microplate photometer as described above, which yielded enzyme activity (ΔAU/s). DMSO was included as blank sample and all measurements were performed in triplicate. The α-amylase inhibition was calculated using the same equation as described for α-glucosidase inhibition.

The PTP1B inhibition assay was performed using 96-well microplates based on a previously reported method (Liang et al., 2021). In short, the sample for each well was dissolved in 18 μL of DMSO and supplemented with 52 μL EDTA solution (3.4 mM in buffer) and 60 μL substrate solution (1.5 mM *p*-NPP and 6 mM DTT in buffer). The buffer (pH 7.0) contains 50 mM Tris, 50 mM Bis-Tris and 100 mM NaCl. The microplate samples were then incubated at 25 °C for 10 min followed by addition of 50 μL PTP1B stock solution (0.001 μg/μL) to each well to initiate the enzymatic reaction after well mixing. The absorbance of the cleavage product formed in each well was measured every 30 s for 10 min at 405 nm, which yielded the enzymatic activity (ΔAU/min). DMSO was included as blank sample and RK-682 as reference compound, and all measurements were performed in triplicate. The PTP1B inhibition was calculated using the same equation as mentioned above. Dose-dependent effect for the PTP1B inhibition assay was determined using the same protocol and the results were expressed as IC_{50} values. Each sample was dissolved in DMSO, followed by two-fold serial dilutions for in total eight or nine concentrations. The initial concentration for dilution series was 2 mg mL^{-1} and 2 mM for the crude leaf extract and pure compounds, respectively. All measurements were performed in triplicate. IC_{50} values were calculated using GraFit software, version 5.0.11 (Erithacus Software Limited) according to the four-parameter function below:

$$f(x) = min + \frac{max - min}{1 + \left(\frac{x}{IC_{50}}\right)^{slope}} \quad \text{(Eq. 2)}$$

where x is the concentration of the sample and slope is the Hill slope, and min is the minimum and max the maximum concentrations for the curves. Results were reported as IC_{50} mean value ± standard error.

4.4. Microfractionation and high-resolution PTP1B inhibition profiling

Microfractionation of the crude acetonitrile extract from the leaves of *E. rigida* was performed on an analytical-scale HPLC with a flow rate of 0.5 mL/min and the temperature maintained at 40 °C. The analytical-scale HPLC was an Agilent 1200 series instrument (Agilent Technologies, Santa Clara, CA, USA) consisting of a G1367C high-performance autosampler, a G1311A quaternary pump, a G1322A degasser, a G1316A thermostatted column compartment, a G1315C photodiode array detector, and a G1364C fraction collector, all controlled by Agilent ChemStation version B.03.02 software. The mobile phase used for the separation was a mixture of different ratio of solvent A (acetonitrile: water: formic acid (5:94.9:0.1, v/v/v)) and solvent B (acetonitrile: water: formic acid (94.9:5:0.1, v/v/v)). For the high-resolution PTP1B inhibition profiling, injection of 10 μL crude extract (50 mg/mL in acetonitrile) was separated on a reversed-phase Phenomenex Luna $C_{18}(2)$ column (150 × 4.6 mm i.d., 3 μm particle size, 100 Å pore size) according to the following gradient: 0 min, 30% B; 30 min,100% B; 40 min, 100% B; 42 min, 30% B; 50 min, 30% B. The eluate from 11 to 42 min was collected into 88 separate wells of a 96-well microplate and the samples were evaporated to dryness by use of a Savant SPD121P speed vacuum concentrator equipped with an OFP400 oil-free pump and an RVT400 refrigerated vapor trap (Holbrook, NY, USA). The dried residue in each well was tested for PTP1B inhibitory activity. The results of percent inhibition for each well sample were plotted against the corresponding retention time of the HPLC chromatogram to construct a high-resolution PTP1B inhibition profile.

4.5. Semipreparative-scale and analytical-scale HPLC separations

Semipreparative-scale HPLC experiments were conducted on a Shimadzu instrument (Tokyo, Japan) consisting of a SIL-20A autosampler, an LC-20AD pump, a CTO-10AS column oven, an SPD-20A UV/VIS detector and an FRC-10A fraction collector, all controlled by Shimadzu LCsolution ver. 1.24 software. Sixteen successive injections of 100 μL (50 mg/mL in acetonitrile) crude acetonitrile extract of *E. rigida* were separated on a Phenomenex Luna $C_{18}(2)$ reversed phase column (250 × 10.0 mm i.d., 5 μm particle size, 100 Å pore size, Phenomenex, Torrance, CA USA) using the same elution gradient profile as for the microfractionation stated above, but with a flow rate of 4 mL/min. This procedure separated peaks *1*–*17* and collected peaks *9* and *10* together as one fraction while other peaks individually as 15 fractions. The representative fractions were frozen in bath of dry ice and acetone and freeze-dried using a Heto LyoPro 6000 freeze dryer. The material eluted with peaks *7* (t_R 26.0 min, 0.72 mg), *12* (t_R 30.9 min, 0.61 mg), and *14* (t_R 32.9 min, 9.89 mg) along with a mixture of peaks *9* and *10* (t_R 28.7/

28.9 min, 1.03 mg) were further purified using the same analytical-scale HPLC instrument as used for microfractionation on a Phenomenex Kinetex PFP column (150 × 4.6 mm i.d., 2.6 μm particle size, 100 Å pore size) by automatic fraction collection. Further purification of the multi-component sample material co-eluting with peak *7* was conducted by dissolving the dried sample material in methanol and 22 successive injections of 12 μL aliquots using the following elution gradient: 0 min, 10% B; 20 min, 100% B; 25 min, 100% B; 26 min, 10% B; 32 min, 10% B. In a similar manner, purification of a mixture of peak *9* and *10* was conducted by 27 successive injections of 10 μL methanol aliquots, for peak *12* by 10 injections of 15 μL methanol aliquots, and for peak *14* by 82 injections of 8 μL methanol aliquots, all using the following elution gradient: 0 min, 30% B; 20 min, 100% B; 25 min, 100% B; 26 min, 30% B; 32 min, 30% B. As a result, 23 pure compounds and one inseparable mixture were isolated. The pure compounds were **1** (t_R 21.1 min, 1.56 mg), **2** (t_R 22.7 min, 1.73 mg), **3** (t_R 23.6 min, 1.93 mg), **4** (t_R 23.9 min, 0.53 mg), **5** (t_R 24.3 min, 0.54 mg), **6** (t_R 25.5 min, 0.41 mg), **7a** (t_R 14.1 min, 0.30 mg), **7b** (t_R 15.3 min, 0.27 mg), **8** (t_R 27.5 min, 0.11 mg), **9** (t_R 28.6 min, 0.60 mg), **10** (t_R 28.9 min, 0.24 mg), **11** (t_R 30.2 min, 1.24 mg), **12a** (t_R 13.9 min, 0.16 mg), **12b** (t_R 14.2 min, 0.08 mg), **12c** (t_R 14.5 min, 0.18 mg), **12d** (t_R 15.0 min, 0.06 mg), **12e** (t_R 15.2 min, 0.04 mg), **13** (t_R 32.3 min, 0.50 mg), **14a** (t_R 14.4 min, 3.72 mg), **14c** (t_R 18.0 min, 1.60 mg), **15** (t_R 34.7 min, 0.80 mg), **16** (t_R 37.8 min, 0.60 mg), and **17** (t_R 40.0 min, 2.64 mg), as well as the inseparable mixture of **14a** and **14b** (t_R 17.6 min, 2.22 mg).

4.5.1. Eremorigidane A (2)

Colorless solid; see Table 2 for ^{1}H (600 MHz) and ^{13}C NMR (150 MHz) spectroscopic data; HRESIMS (negative mode) *m/z* 335.2215 $[M-H]^-$ (calcd for $C_{20}H_{31}O_4^-$ 335.2228, ΔM +3.8 ppm); ECD (*c* 4.43 mM, MeCN) λ_{max} (θ) 190 (+64.95), 206 (+2.48), 302 (+12.20) nm.

4.5.2. .Eremorigidane B (7a)

Colorless solid; see Table 3 for ^{1}H (600 MHz) and ^{13}C NMR (150 MHz) spectroscopic data; HRESIMS (negative mode) *m/z* 335.2233 $[M-H]^-$ (calcd for $C_{20}H_{31}O_4^-$ 335.2228, ΔM −1.5 ppm); ECD (*c* 3.78 mM, MeCN) λ_{max} (θ) 190 (−6.84), 205 (+0.97), 213 (+0.78), 225 (+1.10), 260 (−0.17) nm.

4.5.3. Eremorigidane C (9)

Colorless solid; see Table 3 for ^{1}H (600 MHz) and ^{13}C NMR (150 MHz) spectroscopic data; HRESIMS (negative mode) *m/z* 319.2268 $[M-H]^-$ (calcd for $C_{20}H_{31}O_3^-$ 319.2279, ΔM +3.3 ppm); ECD (*c* 5.46 mM, MeCN) λ_{max} (θ) 190 (−13.14), 203 (−38.31), 222 (−2.13) nm.

4.5.4. Eremorigidane D (14a)

Colorless solid; see Table 2 for ^{1}H (600 MHz) and ^{13}C NMR (150 MHz) spectroscopic data; HRESIMS (negative mode) *m/z* 321.2426 $[M-H]^-$ (calcd for $C_{20}H_{33}O_3^-$ 321.2435, ΔM +2.9 ppm); ECD (*c* 6.51 mM, MeCN) λ_{max} (θ) 190 (+23.88), 204 (+1.97), 216 (+4.49) nm.

4.5.5. Eremorigidane E (14b)

Colorless solid; see Table 2 for ^{1}H (600 MHz) and ^{13}C NMR (150 MHz) spectroscopic data; HRESIMS (negative mode) *m/z* 303.2336 $[M-H]^-$ (calcd for $C_{20}H_{31}O_2^-$ 303.2329, ΔM −2.1 ppm).

4.5.6. Eremorigidane F (14c)

White amorphous solid; see Table 3 for ^{1}H (600 MHz) and ^{13}C NMR (150 MHz) spectroscopic data; HRESIMS (negative mode) *m/z* 303.2341 $[M-H]^-$ (calcd for $C_{20}H_{31}O_2^-$ 303.2329, ΔM −3.8 ppm); ECD (*c* 5.52 mM, MeCN) λ_{max} (θ) 190 (+0.30), 223 (+3.79), 243 (+0.06) nm.

4.6. HPLC-PDA-HRMS analysis

The HPLC-PDA-HRMS analyses were performed on an Agilent 1260 HPLC system (Agilent Technologies, Santa Clara, CA, USA) comprising a G1329B autosampler, a G1316A thermostatted column compartment, a G1315D photodiode array detector and a G1311B quaternary pump with a built-in degasser coupled with a Bruker micrOTOF-Q II mass spectrometer (Bruker Daltonik, Bremen, Germany) equipped with an electrospray ionization source. The operation of the system was controlled by Hystar ver. 3.2 software (Bruker Daltonik, Bremen, Germany). Mass spectra were acquired in negative-ion mode with a capillary voltage of 3500 V, a nebulizer pressure of 2.0 bar, a drying temperature of 200 °C and a drying gas flow of 7 L/min. A solution of sodium formate clusters was injected automatically at the beginning of each analysis to enable internal mass calibration. The crude acetonitrile leaf extract and peaks *7, 12* and *14* as well as a mixture of peaks *9* and *10* were separated using the same column, and an elution gradient profile under the same condition as were used for the analytical-scale HPLC separations respectively as described above.

4.7. NMR experiments

The NMR experiments were performed on a Bruker Avance III 600 MHz NMR spectrometer equipped with a Bruker SampleJet sample changer and a cryogenically cooled gradient inverse triple-resonance 1.7 mm TCI probe-head (Bruker Biospin, Karlsruhe, Germany) at 300 K. The operating frequencies for recording ^{1}H and ^{13}C spectra were 600.13 and 150.90 MHz, respectively. NMR data of **1**–**4**, **6**, **7a**, **7b** and **10** were acquired in methanol-d_4, and for **9**, **14a**-**14c** and **15**–**17** in chloroform-*d*. ^{1}H and ^{13}C chemical shifts were calibrated on the basis of the residual solvent signals, which were δ_H 3.31 ppm/δ_C 49.00 ppm for methanol-d_4 and δ_H 7.26 ppm/δ_C 77.16 ppm for chloroform-*d*. The ^{1}H NMR data were acquired with 30° pulses, an acquisition time of 2.72 s, a relaxation delay of 1.0 s, a spectral width of 20 ppm, and 64 k data points. The ^{13}C NMR data were acquired with 30° pulses, an acquisition time of 0.90 s, a relaxation delay of 2.0 s, a spectral width of 240 ppm, and 64 k data points. Multiplicity edited HSQC spectra were acquired with 12 ppm spectral width for ^{1}H and 170 ppm for ^{13}C. HMBC spectra were also acquired with 12 ppm spectral width for ^{1}H, but 240 ppm for ^{13}C. The relaxation delay for HSQC and HMBC experiments were both 1.0 s. The HMBC, phase-sensitive DQF-COSY and ROESY spectra were all recorded with 2048 whereas the HSQC spectra with 1730 data points in the direct dimension. The HSQC and ROESY spectra were both acquired with 256, whereas the HMBC and COSY spectra with 512 data points in the indirect dimension. Automated NMR data acquisition was controlled by Icon NMR (version 4.2, Bruker Biospin, Karlsruhe, Germany), and the obtained NMR data were processed using Topspin (version 4.0.6, Bruker Biospin).

4.8. Calculation of theoretical ECD spectra and acquisition of experimental ECD spectra

MacroModel interfaced to Schrödinger Maestro 11.9 (Schrödinger, LLC, USA) was used to conduct conformational search with the Merck molecular force field static (MMFFs) in gas phase (Habgood et al., 2020). Density functional theory (DFT) was applied to optimize the conformers within 5.02 kcal/mol of relative energy using B3LYP functional with the 6-31G (d,p) basis set (Pescitelli and Bruhn, 2016). The polarizable continuum model in its integral equation formalism (IEF-PCM) incorporated the solvent effect of acetonitrile (Tomasi et al., 2005). Gaussian 16 program package was used for all DFT and TDDFT calculations, which were performed for each dominant conformer (>1% Boltzmann population) after being optimized (Frisch et al., 2016). TDDFT with the CAM-B3LYP functional and the 6-31G (d,p) basis set was used to calculate oscillator and rotatory strengths of the first 60 excited states of each conformer, including IEF-PCM for the solvent effect of acetonitrile (DTU Computing Center, 2021). The theoretical ECD spectra were generated by Boltzmann averaging the individually calculated ECD spectrum of each dominant conformer. The conformational search and ECD calculations of **7a**, **9** and **14a** were performed for an isomeric form

of model structures **7a-**, **9-** and **14a- model** each after a partial truncation of their structures on the flexible side chain to reduce the computational cost. SpecDis software ver. 1.71 (Berlin, Germany) (Bruhn et al., 2017) was used to export the final theoretical ECD spectra with a half-bandwidth of 0.25 eV for model structure of **7a**, 0.30 eV for **14c** and model structure of **9**, and 0.35 eV for model structure of **14a**.

The JASCO J-1500 CD spectrometer (JASCO, Tokyo, Japan) was used to record experimental ECD spectra of **2**, **7a**, **9**, **14a** and **14c** in acetonitrile in a quartz cuvette (1 cm path length). Acquisition of each spectrum was conducted at 25 °C according to the parameters below: wavelength 190–400 nm, scan speed 50 nm/min, digital integration time 4 s, bandwidth 5.0 mm, 3 accumulations.

CRediT authorship contribution statement

Chao Liang: Writing – review & editing, Writing – original draft, Investigation, Formal analysis, Data curation, Conceptualization. **Chi Ndi:** Writing – review & editing, Methodology, Investigation, Conceptualization. **Susan J. Semple:** Writing – review & editing, Supervision, Investigation, Conceptualization. **Bevan Buirchell:** Writing – review & editing, Methodology, Investigation, Conceptualization. **Sonia Coriani:** Writing – review & editing, Methodology, Investigation, Data curation, Conceptualization. **Birger Lindberg Møller:** Writing – review & editing, Writing – original draft, Supervision, Methodology, Funding acquisition, Conceptualization. **Dan Staerk:** Writing – review & editing, Writing – original draft, Supervision, Software, Resources, Project administration, Methodology, Investigation, Funding acquisition, Formal analysis, Data curation, Conceptualization.

Declaration of competing interest

The authors declare that they have no known competing financial interests or personal relationships that could have appeared to influence the work reported in this paper.

Data availability

Data will be made available on request.

Acknowledgements

HPLC equipment used for high-resolution profiles and purification of compounds was obtained via a grant from The Carlsberg Foundation. The HPLC-PDA-HRMS and NMR instrument were acquired through a grant from “Apotekerfonden af 1991”, The Carlsberg Foundation, and the Danish Agency for Science, Technology and Innovation via the National Research Infrastructure funds. The Novo Nordisk Foundation is acknowledged for support to the project “Desert-loving therapeutics” (grant no. NNF16OC0021616).

Abbreviations

Bis-Tris	bis(2-hydroxyethyl)-imino-tris(hydroxymethylmethane)
CNP-G3	2-chloro-4-nitrophenyl-α-D-maltotrioside
COSY	correlation spectroscopy
DFT	density functional theory
DMSO	dimethyl sulfoxide
DQF	double-quantum filtered
DTT	dithiothreitol
ECD	electronic circular dichroism
EDTA	*N*,*N*,*N*′,*N*′-ethylenediaminetetraacetate
ESI	electrospray ionization
GGDP	(*E*,*E*,*E*)-geranylgeranyl diphosphate
HMBC	heteronuclear multiple-bond correlation
HPLC	high-performance liquid chromatography
HRMS	high-resolution mass spectrometry
HSQC	heteronuclear single quantum coherence
IEF-PCM	integral equation formalism-polarizable continuum model
MMFFs	Merck molecular force field static
NMR	nuclear magnetic resonance
NNDP	(*Z*,*Z*,*Z*)-nerylneryl diphosphate
PDA	photodiode array
PFP	pentafluorophenyl
p-NPG	*p*-nitrophenyl α-D-glucopyranoside
p-NPP	*p*-nitrophenyl phosphate
PTP1B	protein tyrosine phosphatase 1B
ROE	rotating-frame Overhauser
ROESY	rotating-frame Overhauser effect spectroscopy
SAR	structure-activity relationship
SPE	solid phase extraction
TDDFT	time-dependent density functional theory
Tris	tris(hydroxymethyl)-aminomethane
T2D	type 2 diabetes

Appendix A. Supplementary data

Supplementary data to this article can be found online at https://doi.org/10.1016/j.phytochem.2024.113972.

References

Algreiby, A.A., Hammer, K.A., Durmic, Z., Vercoe, P., Flematti, G.R., 2018. Antibacterial compounds from the Australian native plant *Eremophila glabra*. Fitoterapia 126, 45–52. https://doi.org/10.1016/j.fitote.2017.11.008.

Al-Dabbas, M.M., Kitahara, K., Suganuma, T., Hashimoto, F., Tadera, K., 2006. Antioxidant and α-amylase inhibitory compounds from aerial parts of *Varthemia iphionoides* Boiss. Biosci. Biotechnol. Biochem. 70, 2178–2184. https://doi.org/10.1271/bbb.60132.

American Diabetes Association, 2010. Diagnosis and classification of diabetes mellitus. Diabetes Care 33, S62–S69. https://doi.org/10.2337/dc10-S062.

Amina, M., Alam, P., Parvez, M.K., Nawal, M., Al-Musayeib, N.M., Al-Hwaity, S.A., Al-Rashidi, N.S., Al-Dosari, M.S., 2018. Isolation and validated HPTLC analysis of four cytotoxic compounds, including a new sesquiterpene from aerial parts of *Plectranthus cylindraceus*. Nat. Prod. Res. 32, 804–809. https://doi.org/10.1080/14786419.2017.1363750.

Barnes, E.C., Kavanagh, A.M., Ramu, S., Blaskovich, M.A., Cooper, M.A., Davis, R.A., 2013. Antibacterial serrulatane diterpenes from the Australian native plant *Eremophila microtheca*. Phytochemistry 93, 162–169. https://doi.org/10.1016/j.phytochem.2013.02.021.

Biva, I.J., Ndi, C.P., Semple, S.J., Griesser, H.J., 2019. Antibacterial performance of terpenoids from the Australian plant *Eremophila lucida*. Antibiotics 8, 63. https://doi.org/10.3390/antibiotics8020063.

Boschen, N., Goods, M., Wait, R., 2008. Australia’s Eremophilas: Changing Gardens for a Changing Climate. Bloomings Books, Melbourne, p. 160.

Brown, A., Buirchell, B., 2011. A Field Guide to the Eremophilas of Western Australia, first ed. Simon Nevill Publications, Hamilton Hill, W.A, p. 243.

Brown, R.W., 1956. The Composition of Scientific Words. Smithsonian Institution Press, Washington, D.C, p. 753.

Bruhn, T., Schaumlöffel, A., Hemberger, Y., Pecitelli, G., 2017. SpecDis Version 1.71. Berlin, Germany. https://specdis-software.jimdo.com.

Caldwell, C.G., Franzblau, S.G., Suarez, E., Timmermann, B.N., 2000. Oleanane triterpenes from *Junellia tridens*. J. Nat. Prod. 63, 1611–1614. https://doi.org/10.1021/np0002233.

Carroll, P.J., Engelhardt, L.M., Ghisalberti, E.L., Jefferies, P.R., Middleton, E.J., Mori, T. A., White, A.H., 1985. The chemistry of *Eremophila* spp. XXII* New eremane diterpenes from *E. fraseri*. Aust. J. Chem. 38, 1351–1363. https://doi.org/10.1071/CH9851351.

Carrol, P.J., Ghisalberti, E.L., Ralph, D.E., 1976. Tricyclic sesquiterpenes from *Eremophila georgei*. Phytochemistry 15, 777–780. https://doi.org/10.1016/S0031-9422(00)94442-X.

Chatterjee, S., Khunti, K., Davies, M.J., 2017. Type 2 diabetes. Lancet 389, 2239–2251. https://doi.org/10.1016/S0140-6736(17)30058-2.

Chinnock, R.J., 2007. *Eremophila* and Allied Genera: A Monograph of the Plant Family Myoporaceae, first ed. Rosenberg Publishing, Dural, N.S.W.

Chu, C., Li, T., Pedersen, H.A., Kongstad, K.T., Yan, J., Staerk, D., 2019. Antidiabetic constituents of *Dendrobium officinale* as determined by high-resolution profiling of radical scavenging and α-glucosidase and α-amylase inhibition combined with HPLC-PDA-HRMS-SPE-NMR analysis. Phytochem. Lett. 31, 47–52. https://doi.org/10.1016/j.phytol.2019.03.002.

Croft, K.D., Ghisalberti, E.L., Jeferies, P.R., Mori, T.A., Skelton, B.W., White, A.H., 1984. The chemistry of *Eremophila* spp. XXI* Structural study of a new eremane diterpene. Aust. J. Chem. 37, 785–793. https://doi.org/10.1071/CH9840785.

De Munter, S., Köhn, M., Bollen, M., 2012. Challenges and opportunities in the development of protein phosphatase-directed therapeutics. ACS Chem. Biol. 8, 36–45. https://doi.org/10.1021/cb300597g.
DTU Computing Center, 2021. Technical University of Denmark. https://www.hpc.dtu.dk.
Eaton, S.A., Christianson, D.W., 2023. Reprogramming the cyclization cascade of *epi*-isozizaene synthase to generate alternative terpene products. Biochem 62, 2301–2313. https://doi.org/10.1021/acs.biochem.3c00247.
Forgo, P., Zupkó, I., Molnár, J., Vasas, A., Dombi, G., Hohmann, J., 2012. Bioactivity-guided isolation of antiproliferative compounds from *Centaurea jacea* L. Fitoterapia 83, 921–925. https://doi.org/10.1016/j.fitote.2012.04.006.
Forster, P.G., Ghisalberti, E.L., Jefferies, P.R., 1986. The chemistry of *Eremophila* spp. XXVI* new viscidane diterpenes. Aust. J. Chem. 39 https://doi.org/10.1071/CH9862111, 2111-2020.
Forster, P.G., Ghisalberti, E.L., Jefferies, P.R., 1993. Viscidane diterpenes from *Eremophila* species. Phytochemistry 32, 1225–1228. https://doi.org/10.1016/S0031-9422(00)95096-9.
Frisch, M.J., Trucks, G.W., Schlegel, H.B., Scuseria, G.E., Robb, M.A., Cheeseman, J.R., Scalmani, G., Barone, V., Petersson, G.A., Nakatsuji, H., Li, X., Caricato, M., Marenich, A.V., Bloino, J., Janesko, B.G., Gomperts, R., Mennucci, B., Hratchian, H. P., Ortiz, J.V., Izmaylov, A.F., Sonnenberg, J.L., Williams-Young, D., Ding, F., Lipparini, F., Egidi, F., Goings, J., Peng, B., Petrone, A., Henderson, T., Ranasinghe, D., Zakrzewski, V.G., Gao, J., Rega, N., Zheng, G., Liang, W., Hada, M., Ehara, M., Toyota, K., Fukuda, R., Hasegawa, J., Ishida, M., Nakajima, T., Honda, Y., Kitao, O., Nakai, H., Vreven, T., Throssell, K., Montgomery Jr., J.A., Peralta, J.E., Ogliaro, F., Bearpark, M.J., Heyd, J.J., Brothers, E.N., Kudin, K.N., Staroverov, V.N., Keith, T.A., Kobayashi, R., Normand, J., Raghavachari, K., Rendell, A.P., Burant, J. C., Iyengar, S.S., Tomasi, J., Cossi, M., Millam, J.M., Klene, M., Adamo, C., Cammi, R., Ochterski, J.W., Martin, R.L., Morokuma, K., Farkas, O., Foresman, J.B., Fox, D.J., 2016. Gaussian 16, Revision C.01. Gaussian, Inc., Wallingford CT.
Gericke, O., Fowler, R.M., Heskes, A.M., Bayly, M.J., Semple, S.J., Ndi, C.P., Staerk, D., Løland, C.J., Murphy, D.J., Buirchell, B.J., Møller, B.L., 2021. Navigating through chemical space and evolutionary time across the Australian continent in plant genus *Eremophila*. Plant J. 108, 555–578. https://doi.org/10.1111/tpj.15448.
Gericke, O., Hansen, N.L., Pedersen, G.B., Kjaerulff, L., Luo, D., Staerk, D., Møller, B.L., Pateraki, I., Heskes, A.M., 2020. Nerylneryl diphosphate is the precursor of serrulatane, viscidane and cembrane-type diterpenoids in *Eremophila* species. BMC Plant Biol. 20, 91. https://doi.org/10.1186/s12870-020-2293-x.
Ghisalberti, E.L., 1995. The chemistry of unusual terpenoids from the genus *Eremophila*. Stud. Nat. Prod. Chem. 15, 225–287. https://doi.org/10.1016/S1572-5995(06)80133-X.
Ghisalberti, E.L., Jefferies, P.R., Hieu, T.N.V., 1990. Diterpenes from *Eremophila* species. Phytochemistry 29, 316–318. https://doi.org/10.1016/0031-9422(90)89060-M.
Ghisalberti, E.L., Jefferies, P.R., Proudfoot, G.M., 1981. The chemistry of *Eremophila* spp. XV. New acyclic diterpenes from *Eremophila* spp. Aust. J. Chem. 34, 1491–1499. https://doi.org/10.1071/CH9811491.
Habgood, M.J., James, T., Heifetz, A., 2020. Conformational searching with quantum mechanics. In: Heifetz, A. (Ed.), Quantum Mechanics in Drug Discovery. Springer Science+Business Media, LLC, part of Springer Nature, New York, p. 207.
Hansen, N.L., Kjaerulff, L., Heck, Q.K., Forman, V., Staerk, D., Møller, B.L., Andersen-Randberg, J., 2022. *Tripterygium wilfordii* cytochrome P450s catalyze the methyl shift and epoxidations in the biosynthesis of triptonide. Nat. Commun. 13, 5011. https://doi.org/10.1038/s41467-022-32667-5.
Hong, Y.J., Tantillo, D.J., 2014. Branching out from the bisabolyl cation. Unifying mechanistic pathways to barbatene, bazzanene, chamigrene, chamipinene, cumacrene, cuprenene, dunniene, isobazzanene, iso-γ-bisabolene, isochamigrene, laurene, microbiotene, sesquithujene, sesquisabinene, thujopsene, trichodiene, and widdradiene sesquiterpenes. J. Am. Chem. Soc. 136, 2450–2463. https://doi.org/10.1021/ja4106489.
Hong, Y.J., Tantillo, D.J., 2018. A maze of dyotrophic rearrangements and triple shifts: carbocation rearrangements connecting stemarane, stemodene, betaerdene, aphidicolene, and scopadulanol. J. Org. Chem. 83, 3780–3793. https://doi.org/10.1021/acs.joc.8b00138.
Hossain, M.A., Biva, I.J., Kidd, S.E., Whittle, J.D., Griesser, H.J., Coad, B.R., 2019. Antifungal activity in compounds from the Australian desert plant *Eremophila alternifolia* with potency against *Cryptococcus spp*. Antibiotics 8, 34. https://doi.org/10.3390/antibiotics8020034.
Hu, P., Li, D.-H., Jia, C.-C., Liu, Q., Wang, X.-F., Li, Z.-L., Hua, H.-M., 2017. Bioactive constituents from *Vitex negundo* var. *heterophylla* and their antioxidant and α-glucosidase inhibitory activities. J. Funct.Foods 35, 236–244. https://doi.org/10.1016/j.jff.2017.05.047.
Hwang, S.H., Kim, H.-Y., Guillen Quispe, Y.N., Wang, Z., Zuo, G., Lim, S.S., 2019. Aldose reductase, protein glycation inhibitory and antioxidant of Peruvian medicinal plants: the case of *Tanacetum parthenium* L. and its constituents. Molecules 24, 2010. https://doi.org/10.3390/molecules24102010.
International Diabetes Federation, 2021. IDF Diabetes Atlas, tenth ed. Brussels, Belgium. https://diabetesatlas.org/atlas/ninth-edition/.
Johnson, T.O., Ermolieff, J., Jirousek, M.R., 2002. Protein tyrosine phosphatase 1B inhibitors for diabetes. Nat. Rev. Drug Discov. 1, 696–709. https://doi.org/10.1038/nrd895.
Kim, J., Seo, Y.H., Kim, J., Goo, N., Jeong, Y., Bae, H.J., Jung, S.Y., Lee, J., Ryu, J.H., 2020. Casticin ameliorates scopolamine-induced cognitive dysfunction in mice. J. Ethnopharmacol. 259, 112843 https://doi.org/10.1016/j.jep.2020.112843.
Lebovitz, H.E., 1999. Type 2 diabetes: an overview. Clin. Chem. 45, 1339–1345. https://doi.org/10.1093/clinchem/45.8.1339.
Li, C., Wang, S., Yin, X., Guo, A., Xie, K., Chen, D., Sui, S., Han, Y., Liu, J., Chen, R., Dai, J., 2023. Functional characterization and cyclycation mechanism of a diterpene synthase catalyzing the skeleton formation of cephalotane-type diterpenoids. Angew. Chem. Int. Ed., e202306020 https://doi.org/10.1002/anie.202306020.
Liang, C., Kjaerulff, L., Hansen, P.R., Kongstad, K.T., Staerk, D., 2021. Dual high-resolution α-glucosidase and PTP1B inhibition profiling combined with HPLC-PDA-HRMS-SPE-NMR analysis for the identification of potentially antidiabetic chromene meroterpenoids from *Rhododendron capitatum*. J. Nat. Prod. 84, 2454–2467. https://doi.org/10.1021/acs.jnatprod.1c00454.
Liang, C., Ndi, C., Kjaerulff, L., Semple, S., Buirchell, B., Coriani, S., Møller, B.L., Staerk, D., 2023a. Characterization of serrulatane diterpenoids in *Eremophila phyllopoda* subsp. *phyllopoda* by triple high-resolution α-glucosidase/PTP1B/radical scavenging profiling, NMR spectroscopy, DFT-GIAO NMR, and electronic circular dichroism calculations. J. Nat. Prod. 86, 694–709. https://doi.org/10.1021/acs.jnatprod.2c00692.
Liang, C., Staerk, D., Kongstad, K.T., 2020. Potential of *Myrtus communis* Linn. as a bifunctional food: dual high-resolution PTP1B and α-glucosidase inhibition profiling combined with HPLC-HRMS and NMR for identification of antidiabetic triterpenoids and phloroglucinol derivatives. J. Funct.Foods 64, 103623. https://doi.org/10.1016/j.jff.2019.103623.
Liang, C., Zang, J., Ndi, C., Semple, S.J., Buirchell, B., Coriani, S., Møller, B.L., Staerk, D., 2023b. Identification of new PTP1B-inhibiting decipiene diterpenoid esters from *Eremophila clarkei* by high-resolution PTP1B inhibition profiling, enzyme kinetics analysis, and molecular docking. Bioorg. Chem. 139, 106744 https://doi.org/10.1016/j.bioorg.2023.106744.
Liu, G., Xin, Z., Liang, H., Abad-Zapatero, C., Hajduk, P.J., Janowick, D.A., Szczepankiewicz, B.G., Pei, Z., Hutchins, C.W., Ballaron, S.J., 2003. Selective protein tyrosine phosphatase 1B inhibitors: targeting the second phosphotyrosine binding site with noncarboxylic acid-containing ligands. J. Med. Chem. 46, 3437–3440. https://doi.org/10.1021/jm034088d.
Mai, L.H., Chabot, G.G., Grellier, P., Quentin, L., Dumontet, V., Poulain, C., Espindola, L. S., Michel, S., Vo, H.T.B., Deguin, B., Grougnet, R., 2015. Antivascular and anti-parasite activities of natural and hemisynthetic flavonoids from New Caledonian *Gardenia* species (Rubiaceae). Eur. J. Med. Chem. 93, 93–100. https://doi.org/10.1016/j.ejmech.2015.01.012.
Malik, A., Ardalani, H., Anam, S., McNair, L.M., Kromphardt, K.J.K., Frandsen, R.J.N., Franzyk, H., Staerk, D., Kongstad, K.T., 2020. Antidiabetic xanthones with α-glucosidase inhibitory activities from an endophytic *Penicillium canescens*. Fitoterapia 142, 104522. https://doi.org/10.1016/j.fitote.2020.104522.
Pedersen, H.A., Semple, S.J., Buirchell, B., Møller, B.L., Staerk, D., 2020. PTP1B-inhibiting branched-chain fatty acid dimers from *Eremophila oppositifolia* subsp. *angustifolia* identified by high-resolution PTP1B inhibition profiling and HPLC-PDA-HRMS-SPE-NMR analysis. J. Nat. Prod. 83, 1598–1610. https://doi.org/10.1021/acs.jnatprod.0c00070.
Pescitelli, G., Bruhn, T., 2016. Good computational practice in the assignment of absolute configurations by TDDFT calculations of ECD spectra. Chirality 28, 466–474. https://doi.org/10.1002/chir.22600.
Richmond, G.S., Ghisalberti, E.L., 1994. The Australian desert shrub *Eremophila* (myoporaceae): medicinal, cultural, horticultural and phytochemical uses. Econ. Bot. 48, 35–59.
Simpson, B.S., Claudie, D.J., Smith, N.M., Gerber, J.P., McKinnon, R.A., Semple, S.J., 2011. Flavonoids from the leaves and stems of *Dodonaea polyandra*: a Northern Kaanju medicinal plant. Phytochemistry 72, 1883–1888. https://doi.org/10.1016/j.phytochem.2011.05.006.
Singab, A.N., Youssef, F.S., Ashour, M.L., Wink, M., 2013. The genus *Eremophila* (Scrophulariaceae): an ethnobotanical, biological and phytochemical review. J. Pharm. Pharmacol. 65, 1239–1279. https://doi.org/10.1111/jphp.12092.
Syah, Y.M., Ghisalberti, E.L., Skelton, B.W., White, A.H., 1997. A new class of tricyclic diterpenes from *Eremophila georgei* (Myoporaceae). Aust. J. Chem. 50, 705–709. https://doi.org/10.1071/C97043.
Tahtah, Y., Wubshet, S.G., Kongstad, K.T., Heskes, A.M., Pateraki, I., Møller, B.L., Jäger, A.K., Staerk, D., 2016. High-resolution PTP1B inhibition profiling combined with high-performance liquid chromatography-high-resolution mass spectrometry-solid-phase extraction-nuclear magnetic resonance spectroscopy: proof-of-concept and antidiabetic constituents in crude extract of *Eremophila lucida*. Fitoterapia 110, 52–58. https://doi.org/10.1016/j.fitote.2016.02.008.
Tomasi, J., Mennucci, B., Cammi, R., 2005. Quantum mechanical continuum solvation models. Chem. Rev. 105, 2999–3093. https://doi.org/10.1021/cr9904009.
Wang, S.-S., Zhang, Q.-L., Chu, P., Kong, L.-Q., Li, G.-Z., Li, Y.-Q., Yang, L., Zhao, W.-J., Guo, X.-H., Tang, Z.-T., 2020. Synthesis and antitumor activity of α,β-unsaturated carbonyl moiety-containing oleanolic acid derivatives targeting PI3K/AKT/mTOR signaling pathway. Bioorg. Chem. 101, 104036 https://doi.org/10.1016/j.bioorg.2020.104036.
Wubshet, S.G., Tahtah, Y., Heskes, A.M., Kongstad, K.T., Pateraki, I., Hamberger, B., Møller, B.L., Staerk, D., 2016. Identification of PTP1B and α-glucosidase inhibitory serrulatanes from *Eremophila* spp. by combined use of dual high-resolution PTP1B and α-glucosidase inhibition profiling and HPLC-HRMS-SPE-NMR. J. Nat. Prod. 79, 1063–1072. https://doi.org/10.1021/acs.jnatprod.5b01128.
Zhao, Y., Gericke, O., Li, T., Kjaerulff, L., Kongstad, K.T., Heskes, A.M., Møller, B.L., Jørgensen, F.S., Venter, H., Coriani, S., Semple, S.J., Staerk, D., 2023. Polypharmacology-labelled molecular networking: an analytical technology workflow for accelerated identification of multiple bioactive constituents in complex

extracts. Anal. Chem. 95, 4381–4389. https://doi.org/10.1021/acs.analchem.2c04859.

Zhao, Y., Kjaerulff, L., Kongstad, K.T., Heskes, A.M., Møller, B.L., Staerk, D., 2019. 2(5*H*)-Furanone sesquiterpenes from *Eremophila bignoniiflora*: high-resolution inhibition profiling and PTP1B inhibitory activity. Phytochemistry 166, 112054. https://doi.org/10.1016/j.phytochem.2019.112054.

Zhao, Y., Kongstad, K., Jäger, A., Nielsen, J., Staerk, D., 2018. Quadruple high-resolution α-glucosidase/α-amylase/PTP1B/radical scavenging profiling combined with high-performance liquid chromatography-high-resolution mass spectrometry-solid-phase extraction-nuclear magnetic resonance spectroscopy for identification of antidiabetic constituents in crude root bark of *Morus alba* L. J. Chromatogr. A 1556, 55–63. https://doi.org/10.1016/j.chroma.2018.04.041.